Integrated hydrogeophysical modelling and data assimilation for geoelectrical leak detection

Chak-Hau Michael Tso, Lancaster Environment Centre, Lancaster University, Lancaster, UK *

Tim C Johnson, Pacific Northwest National Laboratory, Richland, WA, USA

Xuehang Song, Pacific Northwest National Laboratory, Richland, WA, USA

Xingyuan Chen, Pacific Northwest National Laboratory, Richland, WA, USA

Oliver Kuras, British Geological Survey, Keyworth, UK

Paul Wilkinson, British Geological Survey, Keyworth, UK

Sebastian Uhlemann, British Geological Survey, Keyworth, UK #

Jonathan Chambers, British Geological Survey, Keyworth, UK

Andrew Binley, Lancaster Environment Centre, Lancaster University, Lancaster, UK

*Presently at UK Centre for Ecology & Hydrology, Lancaster, UK

#Presently at Lawrence Berkeley National Laboratory, Berkeley, CA, USA

Corresponding author: m.tso@lancaster.ac.uk , mtso@ceh.ac.uk

Abstract

Time-lapse electrical resistivity tomography (ERT) measurements provide indirect observations of hydrological processes in the Earth's shallow subsurface at high spatial and temporal resolution. ERT has been used in the past decades to detect leaks and monitor the evolution of associated contaminant plumes. Specifically, inverted resistivity images allow visualization of the dynamic changes in the structure of the plume. However, existing methods do not allow the direct estimation of leak parameters (e.g. leak rate, location, etc.) and their uncertainties. We propose an ensemble-based data assimilation framework that evaluates proposed hydrological models against observed time-lapse ERT measurements without directly inverting for the resistivities. Each proposed hydrological model is run through the parallel coupled hydro-geophysical simulation code PFLOTRAN-E4D to obtain simulated ERT measurements. The ensemble of model proposals is then updated using an iterative ensemble smoother. We demonstrate the proposed framework on synthetic and field ERT data from controlled tracer injection experiments. Our results show that the approach allows joint identification of contaminant source location, initial release time, and solute loading from the cross-borehole time-lapse ERT data, alongside with an assessment of uncertainties in these estimates. We demonstrate a reduction in site-wide uncertainty by comparing the prior and posterior plume mass discharges at a selected image plane. This framework is particularly attractive to sites that have previously undergone extensive geological investigation (e.g., nuclear sites). It is well suited to complement ERT imaging and we discuss practical issues in its application to field problems.

Graphical abstract

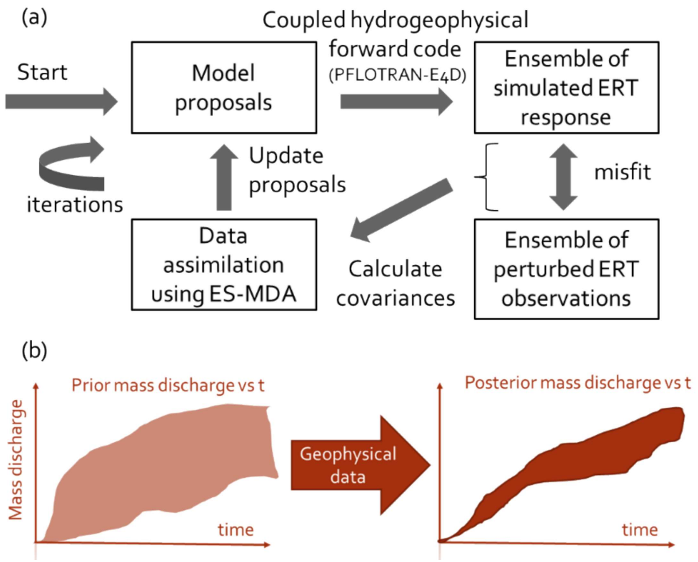

Estimation of leak parameters and their uncertainties using raw geophysical data and data assimilation.

1) Introduction

Identification of solute loadings from an unknown source is a complex yet critical problem. For example, understanding the whereabouts of the source(s) of contamination is often the first question that needs to be addressed in a remediation project. This identification, however, is not straightforward and it is often complicated by factors such as unknown forcing (e.g., boundary and flow conditions), aquifer and vadose zone heterogeneity, and limited data (in terms of number, types, temporal and spatial coverage). Because of these complications, attempts to assess source identification should also address the uncertainties in the estimates, and provide realistic and actionable uncertainty bounds.

Traditional point-based sampling methods suffer from limited coverage and resolution. As prompted, in part, by the wealth of studies in stochastic subsurface hydrology that argued for better field techniques, geophysical methods have emerged as valuable tools for investigating shallow subsurface processes over the past two decades (Binley et al., 2015). Geophysical methods can provide much larger spatial and temporal resolution. Once installed, autonomous long-term monitoring systems, such as ALERT (Kuras et al., 2009), can repeatedly collect geophysical data and transmit it back to the office using telemetry. Among them, electrical resistivity tomography (ERT) is particularly suitable for leak detection due to its sensitivity to fluid conductivity. Note that leak detection is not limited to the detection of the breakthrough of saline fluids (as proxies of contaminants), but it also includes monitoring the integrity of water-retaining structures (e.g. embankments or levees) (Abdulsamad et al., 2019) and landfills (Audebert et al., 2014; Chambers et al., 2006; Maurya et al., 2017). Landfill sites with a high content of inorganics tend to provide good signal (Maurya et al., 2017), which in some cases can be linked to other contaminants from the same source and following the same pathways. However, this is a critical assumption which needs to be tested at each site (Balbarini et al., 2018).Many previous ERT studies have focused on inferring plume characteristics by delineating the plume geometry (Aghasi et al., 2013), obtaining summary statistics of the plume structure (e.g. spatial and temporal movements) (Crestani et al., 2015; Pidlisecky et al., 2011; Singha and Gorelick, 2006), or developing methods for automatic tracking of plumes (Ward et al., 2016). There is also a substantial amount of work dedicated to delineating local hydraulic properties using ERT (e.g. Camporese et al., 2011). As an effort to better use geophysical data for hydrogeological studies, comparisons between coupled and uncoupled hydrogeophysical inversions of ERT-monitored tracer tests have been made (Camporese et al., 2015; Hinnell et al., 2010). Others have tried to address the uncertain link between hydrological systems and geophysical data using data-driven or machine learning approaches (Hermans et al., 2016, 2015; Oware et al., 2013). There is also increased use of geophysics to estimate remediation efficiency (LaBrecque et al., 1996). For example, Power et al. (2014) applied 4D active time-constrained inversion to time-lapse ERT data to estimate the volume of solute plume remediated in a laboratory experiment, while Slater and Binley (2006, 2003) used electrical imaging to monitor the integrity of permeable reactive barriers. Its applicability largely depends whether the plume (e.g. saline or inorganic) and the injected agents (e.g. zero valent iron or oxidants) or background gives distinct electrical signals. Plumes with non-charged compounds, such as chlorinated ethenes, tend not to give an ERT response, except at extreme concentrations. Likewise, in nuclear sites, the concentration of radionuclides itself tend not to generate a large enough signal but secondary species such as metallic ions may give a distinctive ERT response.

The various electrical methods applied to the mapping and monitoring at the U.S. Department of Energy Hanford nuclear site has greatly improved the readiness of these methods (Johnson et al., 2015a). For example, the work on the monitoring of the groundwater/river water interaction beneath the Hanford 300 Area infiltration bonds (Johnson et al., 2012; Johnson et al., 2015b; Slater et al., 2010; Wallin et al., 2013) shows ERT is well suited for monitoring such complex and dynamic processes, while the successful monitoring of vadose zone desiccation (Truex et al., 2013, 2012) at the BC Cribs Area demonstrates its capability to monitor 3-D changes in moisture content caused by gas injection. The leak tank experiments in the 1990s and 2000s have contributed some important work in geoelectrical leak detection. The first two mock tank experiments set up a 15 m diameter steel tank at the Hanford site and ERT tomograms clearly shows area of resistivity decrease of the leak plume (Ramirez et al., 1996). A subsequent series of mock tank experiments evaluated a number of electrical methods for leak detection (Barnett et al., 2003). Among them, a “blind test” was carried out for 110 days where the release episodes were not known to the modeller (Daily et al., 2004). The modeller achieved a 57% success rate in defining a leak or no leak declaration during the test, although further analysis have greatly improved the success rate. A follow-up study on the dataset used Markov chain Monte Carlo inversion to estimate the probability distribution of the plume of being in different sizes and shapes (Ramirez et al., 2005).

In groundwater hydrology or hydrogeophysical problems, models are often too complex (in terms of parameterisation) such that fully Bayesian methods such as Markov chain Monte Carlo (McMC) methods are rarely applied (Irving and Singha, 2010). Data assimilation has played an increasingly important role in subsurface characterization (Zhou et al., 2014). For example, Chen et al. (2013) used p-space ensemble Kalman filter (EnKF) (Nowak, 2009; Schöniger et al., 2012) and ensemble smoother (ES) to assimilate head, flowmeter, and conservative tracer test data to characterize the permeability field of the Hanford 300 area. Zovi et al. (2017) used surface ERT results to generate facies model that honour the geophysical data, then used restart normal-score EnKF to estimate the hydraulic conductivity (K) field. In a recent review, it was concluded that the iterative ES (IES) could achieve results comparable with those of the EnKF, at a fraction of EnKF's computational cost (Li et al., 2018). This computational saving stems from the difference in their formulation—in the EnKF, the data are sequentially integrated into the model at simulation time steps while in ES all the data are combined together and assimilated only once (note in IES the amount of data between updating steps are the same). Since EnKF assimilates data in a sequential fashion (i.e. one time step after another), the number of assimilation steps equals the number of time steps present in the data. Therefore, EnKF is more computationally expensive than IES when data from many time steps are used.

The Hanford leak tank studies and other earlier work on geoelectrical leak monitoring have focused on obtaining time-lapse ERT images during the suspected leak, and making "leak/ no leak" decisions based on the images. It is difficult, however, to use geophysical images to infer leak parameters such as leak location, solute loading, and onset time. Recent hydrogeophysical studies have attempted to estimate parameters of interest from geophysical data without inverting for geophysical images. Different hydrological model proposals are evaluated and compared to observed geophysical data. For example, Manoli et al. (2015) used an iterative particle filter approach and a coupled hydrogeophysical forward model to estimate hydraulic conductivity, K, of up to four zones from ERT data obtained during a controlled infiltration experiment. This approach is then extended to a field study which considers both ERT and ground penetrating radar (GPR) data in K estimation (Rossi et al., 2015). Scholer et al. (2012) used time-lapse crosshole ground GPR data collected under different infiltration conditions to estimate unsaturated soil hydraulic properties using a McMC inversion. Kowalsky et al. (2005) jointly estimated the dielectric and unsaturated zone parameters using both GPR and hydrological data. Johnson et al. (2009) developed a data-domain correlation approach for joint hydrogeological inversion of time-lapse hydrogeological and ERT data to jointly estimate fluid solute concentration and resistivity without explicitly specifying a petrophysical transform.

Though contaminant source identification has been a persistent problem in hydrogeology (Michalak and Shlomi, 2007; Shlomi and Michalak, 2007; Sun, 2007; Sun et al., 2006; Sun and Sun, 2015), advances in data assimilation methods have opened a new avenue in addressing this problem. Only a few studies have jointly estimated leak parameters and hydraulic parameters (Datta et al., 2009; Koch and Nowak, 2016; Wagner, 1992). Zeng et al. (2012) developed a sparse grid Bayesian method for contaminant source identification, which greatly reduced the computational burden in McMC sampling and accurately identifies both leak parameters and time-varying source strengths in case studies. Xu et al. (2016) simultaneously identified the above contaminant source parameters using the restart normal-score ensemble Kalman filter, while subsequently Xu et al. (2018) extended the method to also identify the heterogeneous hydraulic conductivity field. The method has recently been applied to a sandbox study (Chen et al., 2018), where six leak parameters and 2 parameters for the location of an impermeable plate are estimated. Assuming known source location, Kang et al. (2018) estimated K and Dense Non-Aqueous Phase Liquid (DNAPL) saturation (and thus total DNAPL volume) from ERT data using restart EnKF.

In contaminated land studies, there has been a paradigm shift to focus more on site-wide metrics. Instead of focusing on thresholds from point-based measurements, mass discharge and mass flux has been used increasingly (Brusseau and Guo, 2014; Christ et al., 2010, 2006; Hadley and Newell, 2012). Several studies are dedicated to studying their estimation and uncertainty bounds from point measurements (Cai et al., 2011; Troldborg et al., 2012, 2010), while Balbarini et al. (2018) used regression kriging of collocated concentration and geoelectrical data to improve mass discharge estimates.

In this paper, we introduce an ensemble-based data assimilation framework to jointly identify various leak parameters with their associated uncertainty bounds from ERT data. The method evaluates proposed hydrological models (i.e. different hydrogeological units, different leak locations and loads) against observed time-lapse ERT measurements. To the best of our knowledge, this work is the first attempt to estimate solute source parameters using raw ERT data, as most previous work focuses on estimating hydraulic parameters or reconstructing solute distribution. A key feature of our method is that it allows visualization of uncertainty reduction by comparing the envelopes of prior and posterior mass discharge curves. This method is particularly suitable for sites where characterization work had been conducted so that previous results can be used to inform the proposal of prior models. The methods and data used in this work are detailed in section 2. Results of the various synthetic and field test cases are reported in section 3 and 4 respectively. Finally, we discuss and summarize our findings in section 5 and 6 respectively.

2) Methodology

We begin by outlining the different steps in the framework, followed by details of the different framework components. Finally, we introduce the datasets used in test cases.

2.1. Overview of framework

The data assimilation framework (summarized by Figure 1(a)) begins by proposing a range of hydrological models (i.e. model parameters such as leak locations). All parameters for variably saturated flow and transport simulation need to be prescribed, either as a fixed constant or a distribution (which will be updated by the DA framework). Also, the setup for the ERT experiment (e.g. mesh, electrode locations, measurement protocols, petrophysical transforms) need to be included. Once we have an ensemble of model proposals, they are fed to simulate the ERT response using PFLOTRAN-E4D (Johnson et al., 2017). The misfits between observed and simulated ERT responses are used to form data error covariance matrices, which in turn are used to update the model proposals. The entire process repeats until the misfit criterion is met or the algorithm reaches the user-specified maximum number of iterations.

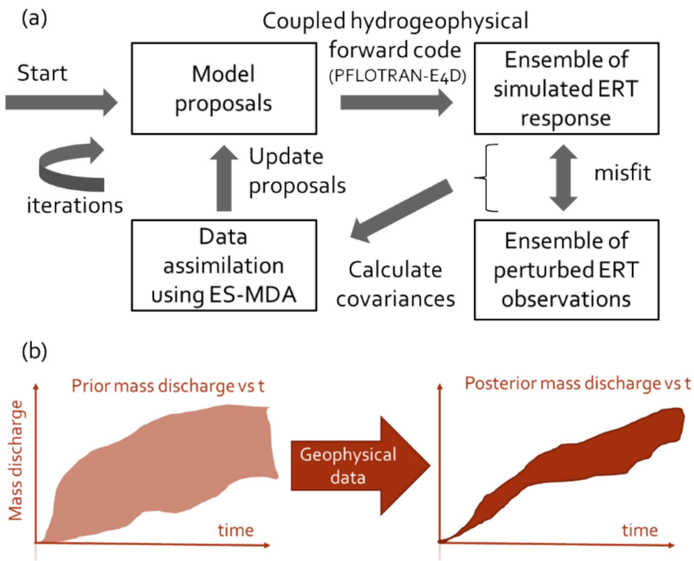

Figure 1 (a) Flowchart of the overall data assimilation framework used in this work. More details are found in the subsections. (b) The goal of this framework is that upon conditioning of geophysical data, the envelope of possible mass discharge time series will become less uncertain.

2.2. Coupled hydrogeophysical forward modelling

We use the massively parallel code PFLOTRAN-E4D (Johnson et al., 2017) for coupled hydrogeophysical forward modelling. E4D (Johnson et al., 2010) is an ERT code which has state-of-the-art capability for parallelization and for accurate modelling of metallic infrastructure (e.g. tanks and pipes that are common at contaminated sites) (Johnson and Wellman, 2015) and near-real-time inversion to monitoring bioremediation (Johnson et al., 2015c). E4D has been used for ERT modelling on a number of complex problems such as those at the Hanford Site. PFLOTRAN (Hammond and Lichtner, 2010 , also see pflotran.org) is a state-of-the-art massively parallel subsurface flow and reactive transport code. PFLTORAN-E4D (implemented as “hydrogeophysics” mode in the 2018 PFLOTRAN distributions used in this work) translates states of the PFLTORAN model to bulk electrical conductivity σ_b distribution using an interpolation matrix that maps between the meshes of the two codes given a petrophysical transform. To do so, users need to provide elementwise petrophysical parameters (e.g. Archie parameters), times when the simulated ERT measurements are needed, and the fluid conductivities of the groundwater and the injected tracer. In this work, we assume surface electrical conductivity is negligible and use Archie’s law as the petrophysical relationship:

$$\sigma_b = \sigma_w \Phi^m S_w^n \tag{1}$$

where m, is the cementation exponent, and n is the saturation exponent. Specifically, fluid conductivity σ_w, porosity Φ , and fluid saturation S_w are passed from the PFLOTRAN output to E4D through the mapping routine. After the petrophysical mapping, E4D will run a forward simulation with the given ERT survey configuration and σ_b distribution to produce the simulated ERT data. Note that PFLOTRAN-E4D is no longer supported in newer PFLOTRAN releases. The mapping routine is available through the corresponding author.

2.3. Prior parameter generation: Latin hypercube sampling

For multi-parameter data assimilation problems, we need to use an efficient scheme to generate $nreaz$ model proposals. We use Latin hypercube sampling (LHS) to obtain multi-parameter model proposals that efficiently span the parameter space. The LHS approach is implemented using the R package *Envstats* (Millard, 2013). For the synthetic and field examples, we assume multivariate Gaussian distribution (N_e= 32) and multivariate uniform distribution (N_e= 64) for the prior distribution of parameter values respectively. The use of more realizations and a non-informative prior in the field example is due to greater parameter uncertainty.

2.4. Data assimilation: ensemble smoother with multiple data assimilation (ES-MDA)

In this work, we use the ensemble smoother with multiple data assimilation (ES-MDA) (Emerick and Reynolds, 2013) to update hydrological models. ES-MDA is also known as an iterative variant of ensemble smoother (ES). The ES-MDA has been used heavily in hydrocarbon reservoir history matching of production and seismic data, but there are growing applications in hydrology. For example, Ju et al. (2018) combined ES-MDA with Gaussian process surrogate modelling and tested the new method on synthetic 2-D transient groundwater flow problems. Lan et al. (2018) combined sequential ensemble-based optimal design and ES-MDA to accurately and efficiently estimate the heterogeneous distribution of physical and geochemical parameters in groundwater models. Aalstad et al. (2018) used ES-MDA and fractional snow-covered area retrieved from satellites to estimate the snow distribution at Arctic sites. Song et al. (2019) used ES-MDA with level set parameterization to estimate the three-facies heterogeneous permeability field at the Hanford IFRC site, while Kang et al. (2019) jointly assimilated ERT and concentration data using ES-MDA alongside with direct sampling (Mariethoz et al., 2010) to estimate the non-Gaussian hydraulic conductivity field from a synthetic salt injection experiment. More recently, a modified version of ES-MDA has been used for crosshole GPR travel-time tomography in conjunction with approximate forward solvers and model error correction (Köpke et al., 2019).

An ensemble smoother (ES) considers all available time-lapse data simultaneously for updating the model parameters. The ES-MDA method essentially allows iterative updating of the nonlinear ES problem by inflating the observational errors by a factor α and solve the updating equation α times iteratively. It has been shown that iterative updating better handles nonlinearity in the data assimilation problem than the classic ES formulation. Our implementation of the ES-MDA procedure is summarized below:

1. Prepare observational data (and their error estimates) to be used for data assimilation (DA)
2. Set up a base PFLOTRAN-E4D model
3. Decide on which parameter(s) to update, either based on expert judgement or some preliminary global sensitivity analysis. The parameter estimation may be affected if important parameters are neither assumed correctly nor updated. Sample N_e realizations from the prior distribution of parameter(s) values (e.g. assume normal or uniform distribution) to obtain parameter array $\boldsymbol{m}$ at $l = 0$ ($\boldsymbol{m}_0$). Parameters that are not being updated are assumed known and base model values are used throughout the DA process for all realizations.
4. Run PFLOTRAN-E4D using $\boldsymbol{m}_0$ to obtain an ensemble of simulated ERT data
5. Updating. For l = 1 to N_a (where N_a is the number of data assimilation steps),
   (i.) The data misfit from the $(l-1)$-th iteration is given by

$$misfit = \frac{\sum_{i=1}^{N_d}\sum_{j=1}^{N_e}(d_{obs,j} - d_{i,j})}{N_e \times N_d} \quad (2)$$

   where N_d is the number of measurements and $d_{i,j}$ is the j-th simulated data of the i-th realization.

   (ii.) Obtain the auto covariance matrix of model predictions $\boldsymbol{C}_{DD}$ and the cross-covariance matrix between the parameter vector and model predictions $\boldsymbol{C}_{MD}$ by

$$\boldsymbol{C}_{DD} = \mathrm{cov}(\boldsymbol{d}^i,\boldsymbol{d}^i) \approx \frac{1}{N_e-1}\sum_{i=1}^{N_e}(\boldsymbol{d}_i - \overline{\boldsymbol{d}})(\boldsymbol{d}_i - \overline{\boldsymbol{d}})^T \quad (3)$$

$$\boldsymbol{C}_{MD} = \mathrm{cov}(\boldsymbol{m}^i,\boldsymbol{d}^i) \approx \frac{1}{N_e-1}\sum_{i=1}^{N_e}(\boldsymbol{m}_i - \overline{\boldsymbol{m}})(\boldsymbol{d}_i - \overline{\boldsymbol{d}})^T \quad (4)$$

where $\boldsymbol{d}_i$ and $\boldsymbol{m}_i$ are vectors of simulated data and model parameter estimates of the i-th realization, respectively. The overbar denotes the mean across realizations of a matrix.

(iii.) For each ensemble member, perturb the observation vector using

$$\boldsymbol{d}_{uc} = \boldsymbol{d}_{obs} + \sqrt{\alpha_l}\boldsymbol{C}_D^{1/2}\boldsymbol{z}_d \tag{5}$$

where α_l is an inflation coefficient, $\boldsymbol{z}_d \sim N(0, \boldsymbol{I}_{N_d})$, $\boldsymbol{I}_{N_d}$ is an identity matrix of size N_d, $\boldsymbol{C}_D$ is the covariance matrix of the measurements error, $\boldsymbol{d}_{obs}$ is a vector of the observed field data. Resampling the vector of perturbed observations at each iteration tends to reduce sampling problems caused by matching outliers that may be generated when perturbing the observations (Emerick and Reynolds, 2013).

(iv.) Update the parameter ensemble using:

$$\boldsymbol{m}_l = \boldsymbol{m}_{l-1} + \underbrace{\boldsymbol{C}_{MD}(\boldsymbol{C}_{DD} + \alpha_l\boldsymbol{C}_D)^{-1}}_{Kalman\ gain}\underbrace{(\boldsymbol{d}_{uc} - \boldsymbol{d}_{l-1})^T}_{misfit} \tag{6}$$

Note that in order to preserve the equivalence between single and multiple data assimilation, it is necessary that $\sum_l^{N_a} 1/\alpha_l = 1$ (Emerick and Reynolds, 2013). This effectively serves to update the average sensitivity matrix.

(v.) Run PFLOTRAN-E4D N_e times using $\boldsymbol{m}_l$to obtain the updated simulated data ensemble

7. If solution does not converge, repeat steps 3-6 with a higher α and/or N_e. Convergence is based on the ensemble root-mean-square-error of the ERT data misfit:

$$RMSE = \sqrt{\frac{1}{N_d}\frac{1}{N_e}\sum_{i=1}^{N_d}\sum_{j=1}^{N_e}\left(d_i^{obs} - d_{i,j}^{sim}\right)} \tag{7}$$

ES-MDA outperforms ES because the smoother effectively represents a single Gauss–Newton iteration with a full step and an average sensitivity matrix (Reynolds et al., 2006) that is approximated by the covariance matrices of the prior ensemble. Instead of a single and potentially large Gauss-Newton correction, ES-MDA allows multiple smaller corrections through the use of multiple iterations and inflating the covariance matrices to damp the parameter updating (Emerick and Reynolds, 2013). It is more flexible and easier to implement than Gauss-Newton methods because it does not require derivation of sensitivity matrices. Previous work have shown that good results can be obtained in a few iterations (e.g. 4-10), while using a decreasing order of α_l's only resulted in small improvements compared to using constant α_l's.

In this work, the above steps (except forward modelling) were implemented in R. For the synthetic studies presented, we set N_a to 7 and use a constant α_i of 7, which appears to obtain convergence in all cases and also satisfies the criterion $\sum_l^{N_a} 1/\alpha_l = 1$. Because the initial misfit for the field data is much larger than that for the synthetic data, the algorithm was unstable and more difficult to converge. Thus, for our field study we set a constant α_l to 200 and iterate until the RMSE is stabilized, which is achieved within ten iterations. Although this violates the $\sum_l^{N_a} 1/\alpha_l = 1$ criterion, we remark that its choice is determined based on data noise levels and discrepancy between observed and simulated data, which can be high in field data. A higher α_l can be seen as adding regularization to the ensemble Kalman scheme (Iglesias, 2016). An alternative approach is to adaptively decide α_i at each iteration automatically (e.g. Le et al., 2016) based on the mean of RMSE of data misfit across all realizations.

In previous hydrogeology applications using ensemble Kalman methods, the hydraulic heads or solute concentrations are often transformed using normal-score transformation (e.g. Schöniger et al., 2012). We consider ERT data to be more Gaussian than hydrogeological data so we use raw ERT data (transfer resistances) directly in this study but such scaling may improve results. Note that the geometric factors for the crosshole measurements in our examples do not vary greatly.

2.5. Plume mass discharge

Mass discharge is the integral of solute fluxes across a control plane (ITRC, 2010). The control plane can be a model or site boundary, the water table, or any arbitrary planes. Mass flux is defined as $J = q_0 C$, where is q_0 groundwater flux and C is solute concentration. It follows that the solute mass discharge (or equivalently solute integral flux) across a control plane is defined as $M_d = \int_A J dA$, where A is area of the control plane and J is the spatially variable solute mass flux. Note that since the solute fluxes are vectors, it is possible for solute mass discharge to be negative. As shown in Figure 1(b), one way to visualize reduction in site-wide uncertainty is by observing a reduction of spread of the mass discharge time series.

3) Synthetic experiments based on the Sellafield ERT field trial

Between 2013-2014, a field ERT trial was conducted at the Sellafield Nuclear Site in Cumbria, U.K. (Kuras et al., 2016; Tso et al., 2017) by the British Geological Survey to demonstrate the utility of a permanent ERT monitoring system to support critical decommissioning activities at nuclear sites. Four vertical boreholes and two inclined boreholes with forty electrodes each were installed in front of the Sellafield MSSS building. The field trial included three controlled injections of an electrically conductive tracer (as simulant of the silo liquor) into the vadose zone. Time-lapse ERT data were collected during the experiment.

We built a PFLOTRAN model based on the hydrogeological model developed for Sellafield (Kwong and Fowler, 2014) and an E4D model based on the electrode locations and design of the field trial. Details of the PFLOTRAN and E4D models are found in Table 1. Note that there are multiple units in the domain, but only the hydraulic parameters in the main unit (i.e. sandy drift) is listed in Table 1. The parameters not being estimated are kept constant during parameter estimation.

To test our method, we obtained synthetic ERT data based on the experimental setup of the field trial and consider a series of parameter estimation cases. They are summarized in Table 2. Unless otherwise stated, the parameters not being estimated are assumed to be known exactly. We began by considering the estimation of leak location ($xloc$,$yloc$), both for a leak inside and outside the ERT monitoring cell. Then we proceed by also estimating the solute loading (q), release onset time (t_0). Subsequently, we estimate both leak parameters and uniform Archie parameters (m,n) jointly, which is important in field applications as fixing the parameters imposes too much confidence on uncertain petrophysical relationships. Finally, we consider a few cases with uncertainty and heterogeneity in hydraulic conductivity (K). In the first case, the K field has a log variance of 1.0 but its mean value is unknown; while in the second case, the K field is heterogeneous but its mean value is known. In the last case, the mean K value is being estimated for a heterogeneous field. Other potential parameters to consider includes water table depths, permeability [log10 (m^2)], porosity, unsaturated zone van Genuchten parameters, recharge rates, depth of the leak ($zloc$), and duration of the leak (dt). Each iteration takes 40 minutes on average to run on 192 cores on PNNL's institutional computing facility. Note that only the forward modelling is parallelized, not the parameter updating.

Table 1 "True" coupled hydrogeophysical model parameters used for synthetic experiments. It is developed based on the Sellafield field trial. *Only parameters for the main zone are listed below. #Leak location for some cases is (33.4534, -14.4303) instead. Note that for all cases the leak location is at the water table.

PFLOTRAN simulation	Value
Total simulation time (days)	30
Model dimensions (m)	40 x 40 x 20
Grid spacing (m)	1 x 1 x 1
Horizontal permeability (m^2) *	8.8854 x 10^{-10}
Vertical permeability (m^2) *	4.4427 x 10^{-11}
Porosity *	0.2
Water table depth (m)	6.0
van Genuchten m	0.5
van Genuchten α	1 x 10^{-4}
Residual water saturation	0.1
Leak location (m) #	(20,-10,18.1)
Leak period (day)	12-30
Leak rate (m^3/d)	8.0
Background fluid conductivity (S/m)	1 x 10^{-4}
Leak fluid conductivity (S/m)	0.1
Mass discharge plane	Vertical plane at y=-25.03m
E4D simulation	**Value**
Full Model dimensions (m)	100 x 100 x 100
Imaging cell dimensions (m)	9.5 x 22.8 x 41.5
Grid spacing	Unstructured
Number of elements	380457
ERT imaging times (day)	Every 5 days between day 5 to day 30
Archie's cementation exponent	1.3
Archie's saturation exponent	2.0

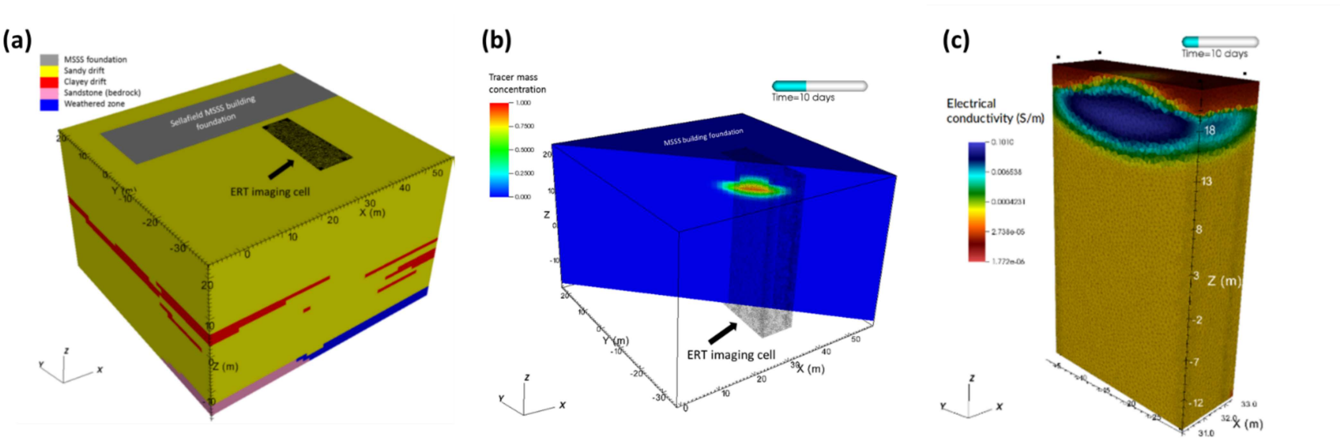

Figure 2 . (a) PFLOTRAN model domain for the Sellafield MSSS. The grey area is the MSSS building, which is modelled as impermeable. The hashed area is the ERT imaging cell consisting of four ERT boreholes. (b) A snapshot of the simulated tracer concentration due to injection. (c) The corresponding distribution of electrical conductivity within the ERT imaging cell obtained via petrophysical transform.

Table 2 Summary of synthetic cases. All cases converge in seven iterations.

Figure	Size of ensemble (N_e)	Parameter(s) to estimate	Prior distribution	Comments	Initial and final RMSE
Figure 3a	32	$xloc$, $yloc$	6x6 grid (exclude corners) Uniform spacing X range: -5 – 55m Y range: -33 - -3m	Estimation of the leak location on the x,y plane ; leak is located within the ERT cell	3.63 → 1.01
Figure 3b	32	$xloc$, $yloc$	6x6 grid (exclude corners) Uniform spacing X range: -5 – 55m Y range: -33 - -3m	Estimation of the leak location on the x,y plane; leak location is outside the ERT cell	7.66 → 1.01
Figure 4	32	$xloc$, $yloc$,q, $t0$	Multivariate uncorrelated truncated Gaussian: xloc = (mean=25.0, sd=20.0, min=-5.0,max=55.0), yloc = (mean=-18.0,sd=10.0,min=-33.0, max=-3.0), q = (mean=15.0,sd=10.0,min=0.0, max=30.0), t0 = (mean=15.0,sd=10.0,min=0.0, max=30.0)	Estimation of the 4 leak parameters	7.01 → 1.01
Figure 5	32	$xloc$, $yloc$,q, $t0$, m, n	Multivariate uncorrelated truncated Gaussian: xloc = (mean=25.0, sd=20.0, min=-5.0,max=55.0), yloc = (mean=-18.0,sd=10.0,min=-33.0, max=-3.0), q = (mean=15.0,sd=10.0,min=0.0, max=30.0), t0 = (mean=15.0,sd=10.0,min=0.0, max=30.0), c = (mean=1.6,sd=0.5,min=0.0, max=2.0), m = (mean=2.5,sd=0.8,min=0.0, max=3.0)	Joint estimation of leak parameters and uncertain (homogeneous) petrophysical parameters (Archies cementation factor and saturation exponent)	22.65 → 1.65
Figure 6a	32	$xloc$, $yloc$,q, $t0$	Multivariate uncorrelated truncated Gaussian: xloc = (mean=25.0, sd=20.0, min=-5.0,max=55.0), yloc = (mean=-18.0,sd=10.0,min=-33.0, max=-3.0), q = (mean=15.0,sd=10.0,min=0.0, max=30.0), t0 = (mean=15.0,sd=10.0,min=0.0, max=30.0)	Leak estimation under the influence of permeability heterogeneity	3.30 → 1.10
Figure 6b	32	$xloc$, $yloc$,q, $t0$	Multivariate uncorrelated truncated Gaussian: xloc = (mean=25.0, sd=20.0, min=-5.0,max=55.0), yloc = (mean=-18.0,sd=10.0,min=-33.0, max=-3.0), q = (mean=15.0,sd=10.0,min=0.0, max=30.0), t0 = (mean=15.0,sd=10.0,min=0.0, max=30.0)	Leak estimation under the influence of and uncertain (homogeneous) permeability	6.47 → 1.31 6.66 → 1.70 6.50 → 1.22 6.53 → 1.41 6.54 → 1.27
Figure 7	32	$xloc$, $yloc$,q, $t0$, K	Multivariate uncorrelated truncated Gaussian: xloc = (mean=25.0, sd=20.0, min=-5.0,max=55.0), yloc = (mean=-18.0,sd=10.0,min=-33.0, max=-3.0), q = (mean=15.0,sd=10.0,min=0.0, max=30.0), t0 = (mean=15.0,sd=10.0,min=0.0, max=30.0), K = (mean=-9.0,sd=sqrt(1.0),min=-11.0, max=-7.0))	Joint estimation of leak parameters and uncertain (homogeneous) permeability values	3.30 → 1.03

3.1. Base cases

Our initial example considers the estimation of the leak location (Figure 3). The prior realizations are laid in a rectangular grid. We consider both the cases where the leak is within and outside the ERT imaging cell. Although the estimate at the first iteration is superior when the leak is within the imaging cell, the leak location is accurately estimated after seven iterations in both cases. Figure 4 shows the results from the joint estimation of four leak parameters: the (x,y) coordinates of the leak location, leak rate, and onset time, assuming a wide multivariate Gaussian prior distribution. After conditioning the parameter values with ERT data, all four leak parameters are accurately estimated. Figure 4b shows the mass discharge curves across a pre-defined plane. The mass discharge curves for the prior distribution are highly variable, while those for posterior distribution collapse to the true curve.

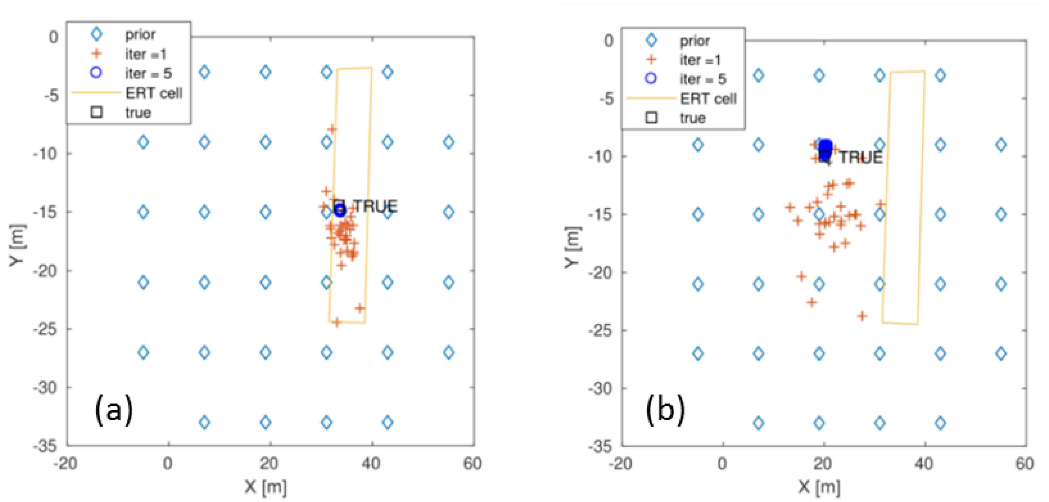

Figure 3 Estimation of leak location. (a) The true leak location is within the ERT array (33.4534, -14.4303). (b) The true leak location is outside the ERT array (20, -10). In both cases, the data assimilation framework successfully identified the true leak location within a few iterations.

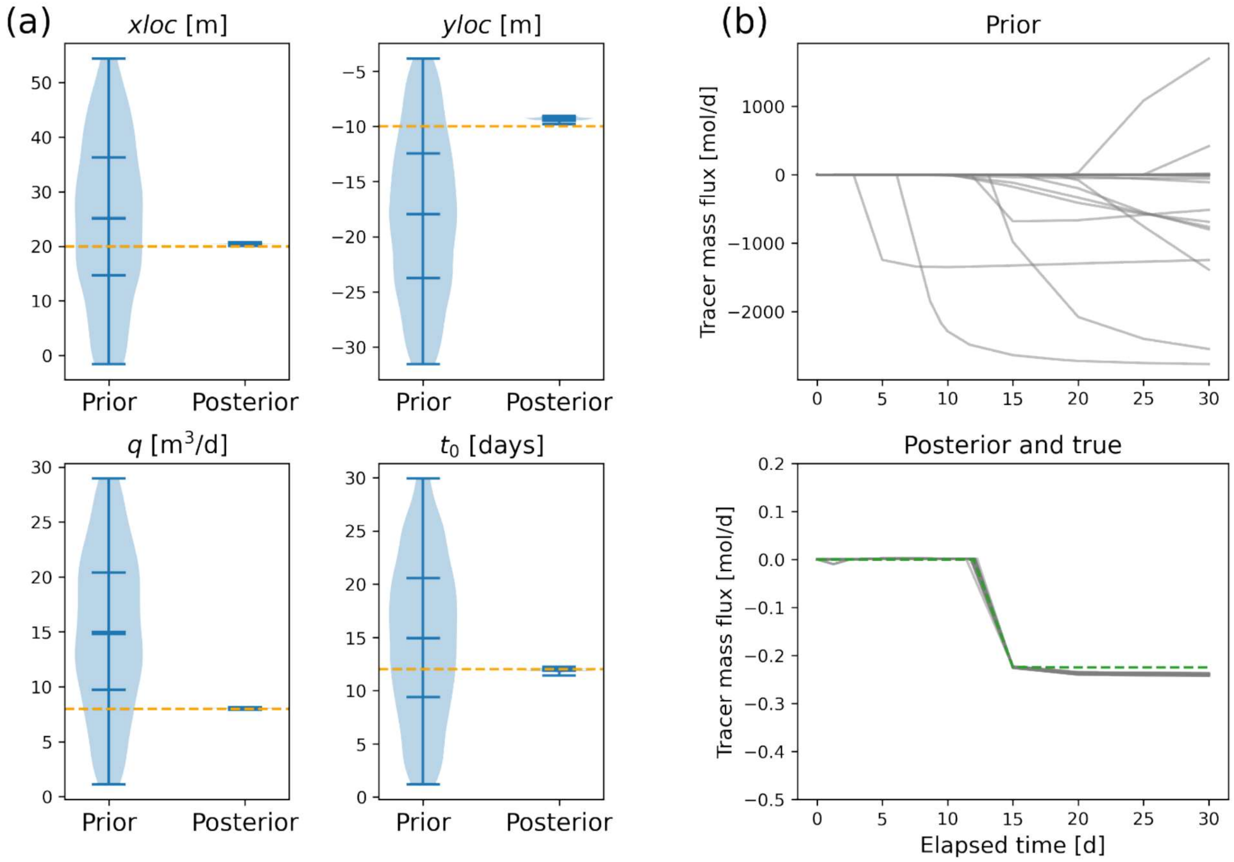

Figure 4 Joint estimation of leak parameters: (x,y) location, leak rate, and onset time. (a) Violin plots showing the prior and posterior parameter distributions. In each violin plot in this paper, the minima, maxima, mean, median, as well as the 25% and 75% quantiles are marked. The true values are marked with an orange lines. The posterior parameter values collapse around the true values (b) Prior and posterior tracer mass discharge (i.e. integral of mass fluxes) across the pre-defined plane. All the posterior curves collapse to nearly the true curve (green). Note that the sign of mass discharge denotes its direction across the plane.

3.2. Effects of petrophysical parameters

Figure 5 shows the joint estimation of leak parameters and Archie petrophysical parameters. The prior estimates are generated as multivariate Gaussian distributions using Latin hypercube sampling. The posterior estimates are in very good agreement with the true values, with the exception that the onset time is slightly underestimated. It is noteworthy that including the Archie parameters as a covariate has caused the RMSE of the prior ensemble to be much higher than those in other synthetic test cases (see Table 2), highlighting that it causes a larger range of transfer resistance values.

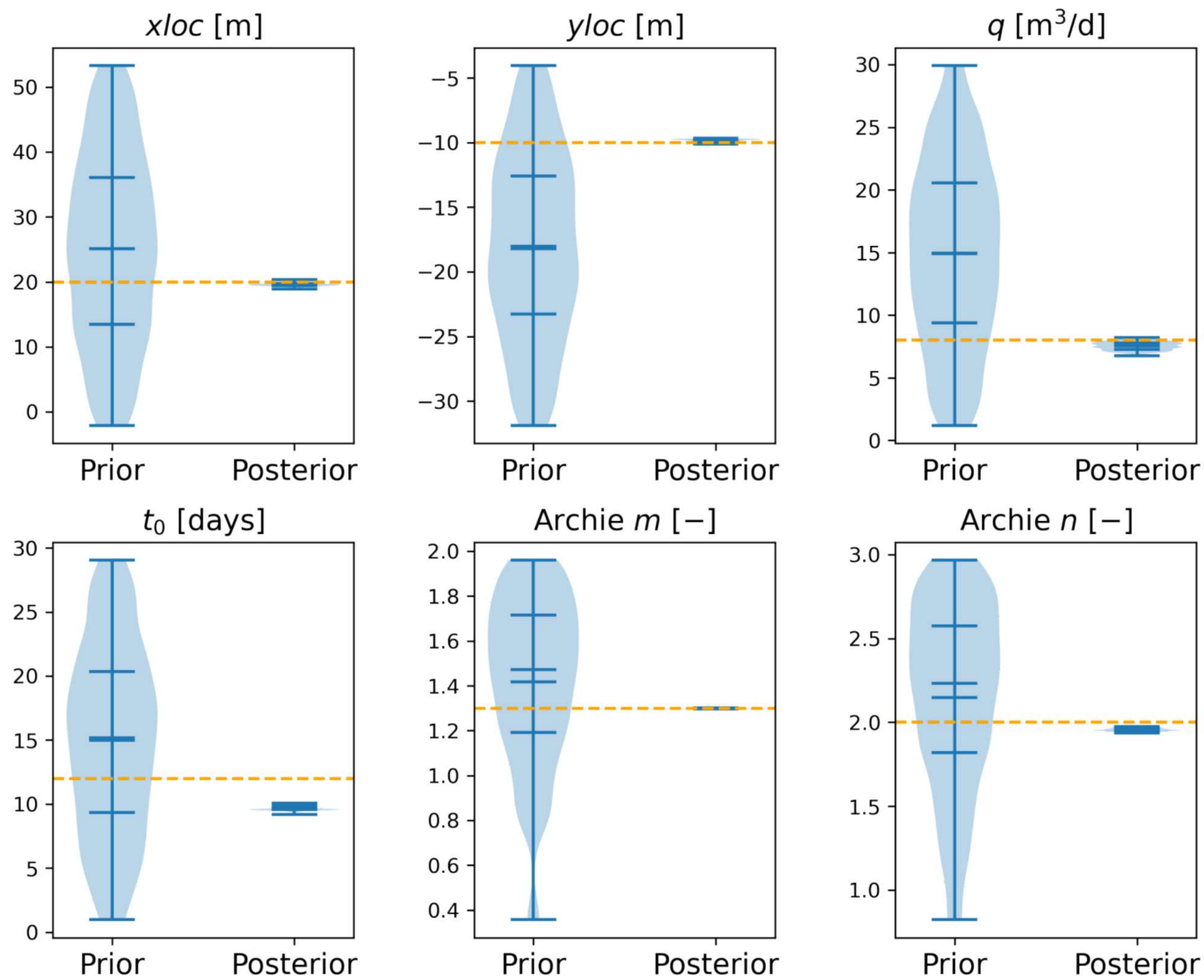

Figure 5 Joint estimation of leak and petrophysical parameters: the prior and posterior parameter distributions are shown as violin plots. The true values are marked with orange lines.

3.3. Influence and joint estimation of uncertain (homogeneous) hydraulic conductivity

Figure 6a shows the estimation of leak parameters under uncertain K values. Estimating leak parameters under K uncertainty leads to highly uncertain and inaccurate leak parameter estimates. Figure 6b shows the estimation of leak parameters with variance of log K equal to 2, 3, 5, 7, 10, while assuming the mean K values are known exactly and unit correlation lengths. Although some variations in the estimates are seen, they generally lie close to the true values. There is no apparent correlation between the leak parameter estimation performance and the variance of the field. Figure 7 shows the estimates of leak parameters and effective hydraulic conductivity. The results show good estimates of the leak locations, while that for q and t_0 is manifested as a narrow envelope. The posterior uncertainty for K remains high and the algorithm underestimates the effective K value. Again, the envelope of mass discharge curves is greatly reduced, demonstrating a reduction in uncertainty. However, the posterior curves do not collapse to the true curve, indicating significant uncertainty in the estimates.

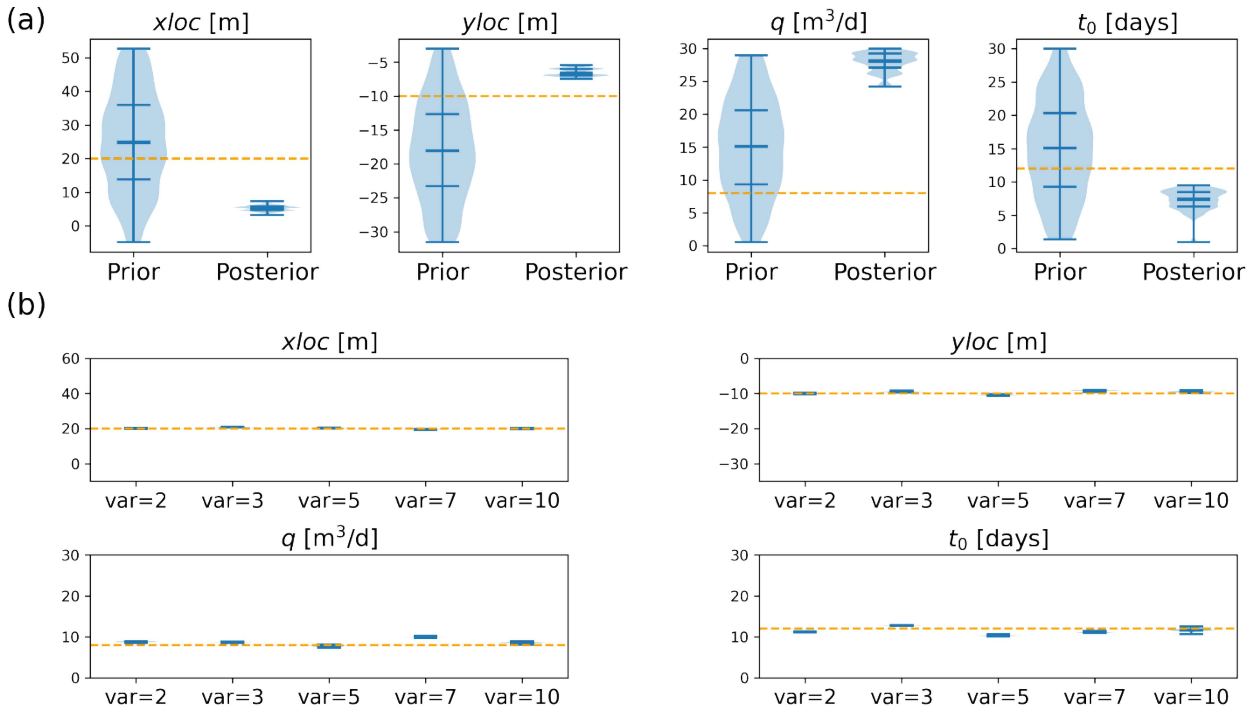

Figure 6 (a) The estimation leak parameters under uncertain K values and K (log10) variance = 1.0. The violin plots show the prior and posterior parameter distributions. The true value is marked with an orange line. (b) The estimation of leak parameters at variance of log10(K) equal to 2, 3, 5, 7, 10 , while assuming the mean K values are known exactly and the K field is isotropic and is of unit correlation length. The violin plots show the posterior parameter distribution, while the true value is marked with an orange line.

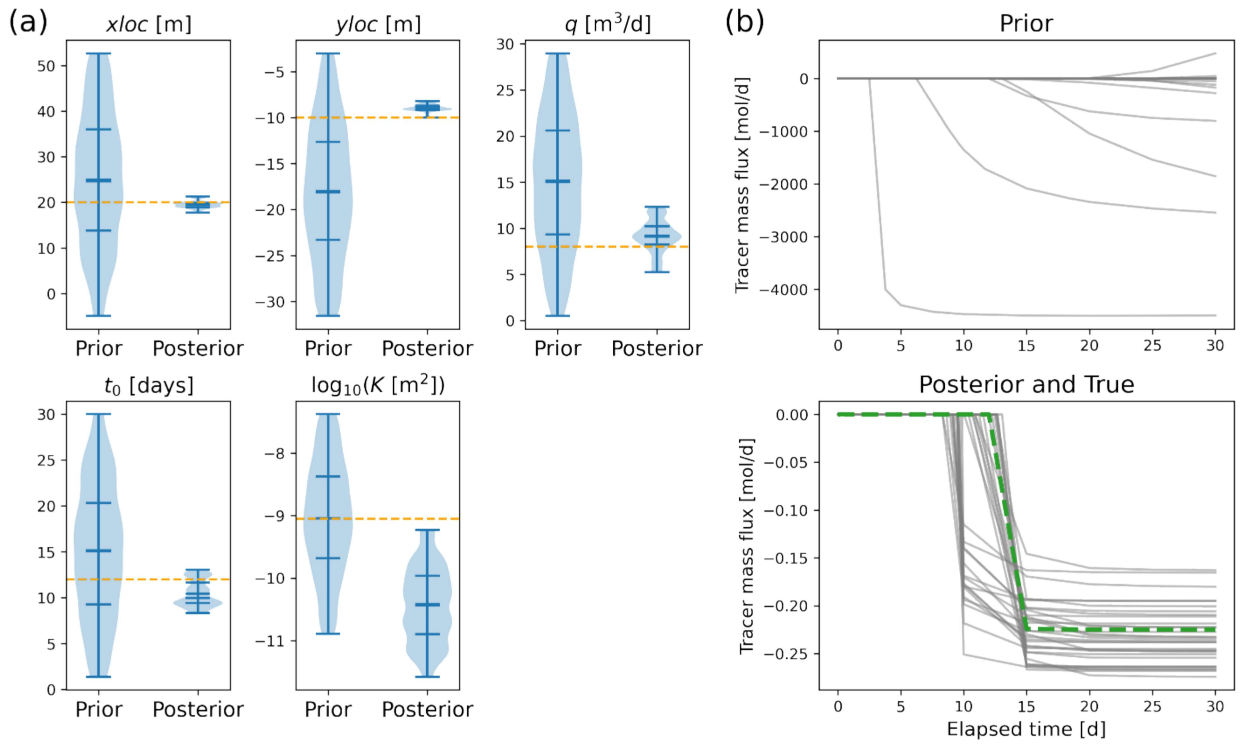

Figure 7 (a) Joint estimation of leak parameters and effective hydraulic conductivity. The violin plots show the prior and posterior parameter distributions. The true value is marked with an orange line. (b) Prior and posterior tracer mass discharge across the pre-defined plane. The true curve is marked in green in the posterior plot.

4) Field application at the Hatfield site

4.1. Data description

To illustrate the approach in a field setting we use data from a solute injection experiment at the Hatfield (Yorkshire) site in the UK. At the site, six boreholes were drilled in 1998 in order to monitor tracer injection, two of which were for transmission GPR measurements (H-R1 and H-R2), while four were for ERT measurements (H-E1, H-E2, H-E3, and H-E4). These four ERT boreholes consist of sixteen stainless steel mesh electrodes equally spaced between 2 and 13 m depth. These boreholes were drilled to a depth of 12 m and completed with 75 mm PVC casing. Both the ERT and radar boreholes have a weak sand/cement grout backfilling the annulus. A tracer injection borehole was also installed (H-I2), located within the centre of the borehole array. The injection borehole is 3.5 m deep, with a 100 mm diameter slotted section and gravel pack between 3 and 3.5 m depth.

We focus our discussion using the ERT results from the March 2003 tracer infiltration experiment at Hatfield (Winship et al., 2006). The tracer consisted of 1,200 litres of water, dosed with NaCl to give an electrical conductivity value of 2200 µS cm^{-1} (groundwater electrical conductivity at the site was measured as 650 µS cm^{-1}). The tracer was injected over a period of three days, from 14th March 2003 to 17th March 2003 at a steady rate of approximately 17 litres per hour. A float valve in the injection borehole was used to control the head in the injection borehole, and hence the flow rate. Duplicate sets of background measurements of ERT were made on 6th March and 13th March. Tracer flow was monitored by means of a pressure transducer in a storage tank, which gave a way of calculating the cumulative injection volume over time. The tracer injection port H-I2 was screened between 3m and 3.5m below ground surface. The tracer injection was monitored by ERT measurements from four boreholes and inverted images clearly show the plume migration, as shown in Figure 8 (Winship et al., 2006). During the tracer test no rainfall was observed at the site. The water table was observed at approximately 10 m depth.

After removal of outliers, 3108 of the 3172 measurements are kept and 5% Gaussian data error is assumed in the inversions. Let $t = 8$ be the day where injection commenced, ERT snapshots for $t = 7, 10, 15, 21$ days are used in the inversion. Table 3 lists the baseline parameters for our simulation, which are largely adopted from Binley et al. (2002). The parameters not being estimated are kept constant during parameter estimation.

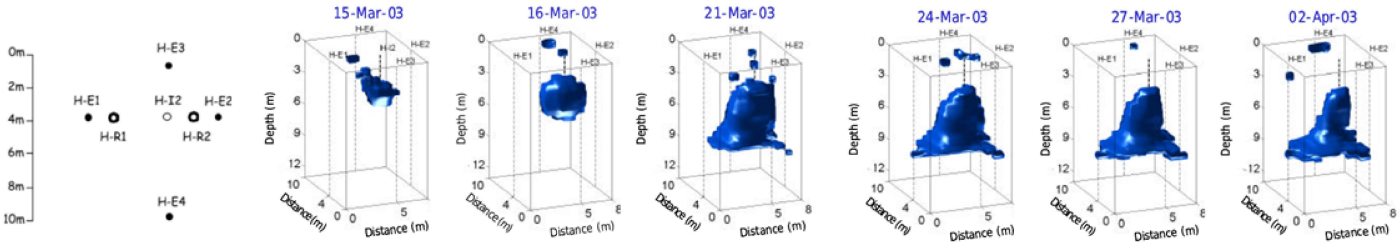

Figure 8 Setup of the tracer injection test at Hatfield (H-I2 is the injection borehole and H-E1 to H-E4 are ERT boreholes) and the time-lapse resistivity images (iso-surfaces are plotted for 7.5% reduction of resistivity relative to baseline) obtained from a difference inversion of the ERT data (reproduced from Winship et al., 2006)

Table 3 Baseline coupled hydrogeophysical model parameters used for the parameter estimation from the Hatfield field ERT data. *The domain consists of 3 meters of top soil and a uniform main zone. Only parameters of the main zone are listed below.

PFLOTRAN simulation	Value
Total simulation time (days)	41
Model dimensions (m)	30 x 33 x 16
Grid spacing (m)	1 x 1 x 0.5
Permeability (m^2) *	4.8225 x 10^{-13}
Porosity *	0.32
Water table depth (m)	-12.0
van Genuchten m *	0.6
van Genuchten α *	3.5 x 10^{-3}
Residual water saturation *	0.04
Recharge (m/day)	1 x 10^{-4}
Leak location (m)	(3.0, 4.0,-3.0)
Leak period (day)	8-11
Leak rate (m^3/d)	0.408
Background fluid conductivity (S/m)	0.22
Leak fluid conductivity (S/m)	0.065
Mass discharge plane	Vertical plane at y = -3 m
E4D simulation	**Value**
Full Model dimensions (m)	500 x 500 x 50
Imaging cell dimensions (m)	10 x 13 x 15
Grid spacing	Unstructured
Number of elements	46482
ERT imaging times (day) for inversion	7, 10, 15, 21
Archie's cementation exponent	1.35
Archie's saturation exponent	1.35

4.2. Parameter estimation

We applied the proposed leak detection framework to the Hatfield field data and consider two cases (details are listed in

Table 4). The first case estimates four leak parameters and two Archie parameters ($xloc, yloc, \log q, t0, m, n$). The second case considers the estimation of a few additional parameters, namely the duration of the leak event (dt) and the uniform horizontal and vertical hydraulic conductivity (K and Kz). We consider K anisotropy may exist at the site because well logs suggest the presence of fine-texturedlayers (Binley et al., 2001). Compared to the earlier synthetic examples, convergence was much more difficult to achieve. We have used the following modification to our methods to circumvent this issue: we estimated $\log q$ instead of q, used more realizations, and used a uniform prior instead of a Gaussian one. We transformed the leak location priors to a uniform grid to aid the interpretation of the results. We have not considered the estimation of depth of the leak source in any of our examples because for most leak detection problems, the leak depth is usually precisely known: for example, base of storage tanks/silos, depth of buried pipelines, and bottom of landfill lining. Each iteration takes 2.5 hours on average to run on 192 cores. Note that only the forward modelling is parallelized, not the parameter updating.

Results from the base case is reported in Figure 9. Figure 9(a) shows that the posterior estimates of most parameter pairs form a small cluster. The estimates of $xloc$ and $\log q$ are close to the true values, while those for $yloc$ and t_0 are slightly above the true (known) values. The inversion appears to have no sensitivity to m, while the estimation of n converges to a very small value of about 0.53. Note that in this field test the true values of m and n are not known. In the inversion of field data, we would not necessarily consider the estimates of m and n representative of actual petrophysical parameters, but rather they act as hyperparameters to adjust any discrepancy in model structure. Figure 9(b) shows that the variability of mass discharge curves between realizations is greatly reduced upon conditioning of ERT data. Specifically, its spread is reduced by two orders of magnitude, highlighting a reduction in site-wide uncertainty of the plume migration.

Results from the second case are reported in Figure 10. We observe a larger spread in the parameter space but similar results for the estimation of m and n. $xloc$, $yloc$, and t_0 are slightly overestimated. The inversion appears to have no sensitivity to K and Kz. The estimates of $\log q$ and dt centres around the true value, indicating the inversion algorithm also correctly estimates the total solute loading ($q \times dt$) that enters the flow and transport modelling domain. This underscores that the proposed data assimilation framework does not suffer from mass balance issues that are common in inverted resistivity-based approaches.

Table 4 Summary of cases for the Hatfield field example

Figure	Size of ensemble (N_e)	Parameter(s) to estimate	Prior distribution	Comments	Final RMSE
Figure 9	64	$xloc$, $yloc$, $\log q$, $t0$, m, n	Multivariate uncorrelated uniform: Adjusted uniform grid from $xloc$ 0-8m and $yloc$ =0-10m $\log q$= list(min=-2.0, max=1.0), $t0$= list(min=0.0, max=20.0), m = list(min=0.5, max=2.5), n = list(min=0.5, max=2.5)	Base case	223.16→15.3 (iter=8, stabilized afterwards)
Figure 10	64	$xloc$, $yloc$, $\log q$, $t0$, dt m, n, K, Kz	Multivariate uncorrelated uniform: Adjusted uniform grid from $xloc$ 0-8m and $yloc$ =0-10m $\log q$= list(min=-2.0, max=1.0), $t0$= list(min=0.0, max=20.0), dt = list(min=1.0, max=5.0), m = list(min=0.5, max=2.5), n = list(min=0.5, max=2.5), K = list(min=-13.0, max=-9.0), Kz = list(min=-13.0, max=-9.0)	K, Kz, and dt are also estimated.	310.66→13.95 (iter = 2, stabilized afterwards)

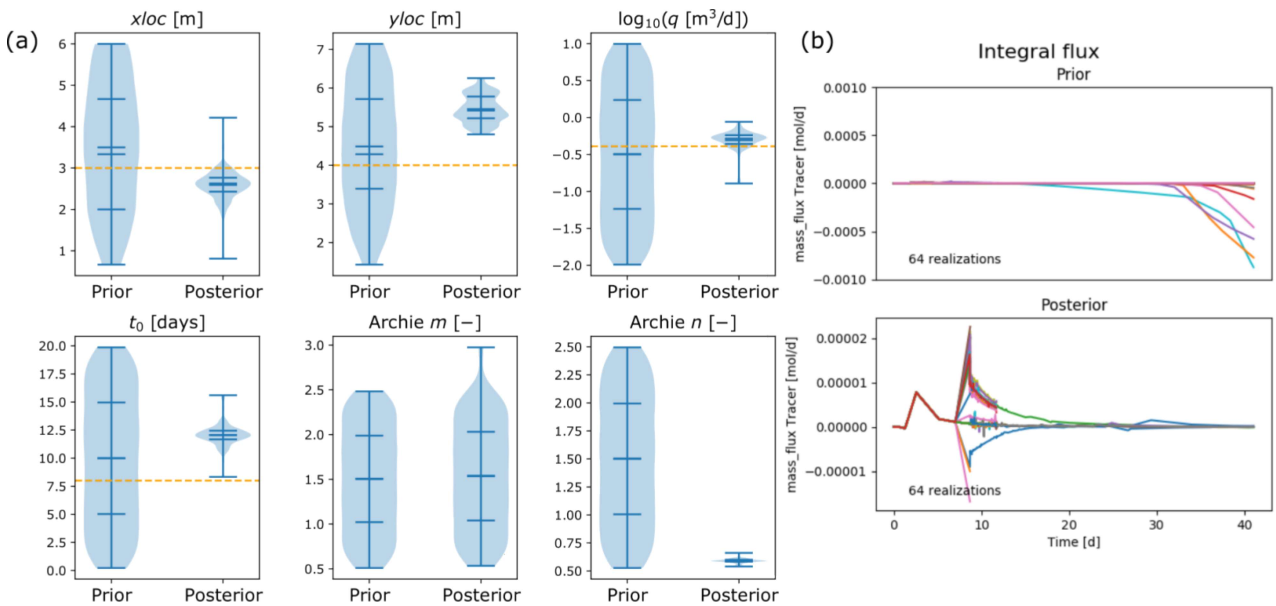

Figure 9 (a) Violin plots showing the prior and posterior parameter values for the Hatfield example estimating leak and Archie parameters. The parameter symbols are defined in section 3. The true leak parameters used in the field injection experiment is indicated by the orange lines. (b) The prior and posterior mass discharge time series. The sign of mass discharge indicates the direction across the defined plane.

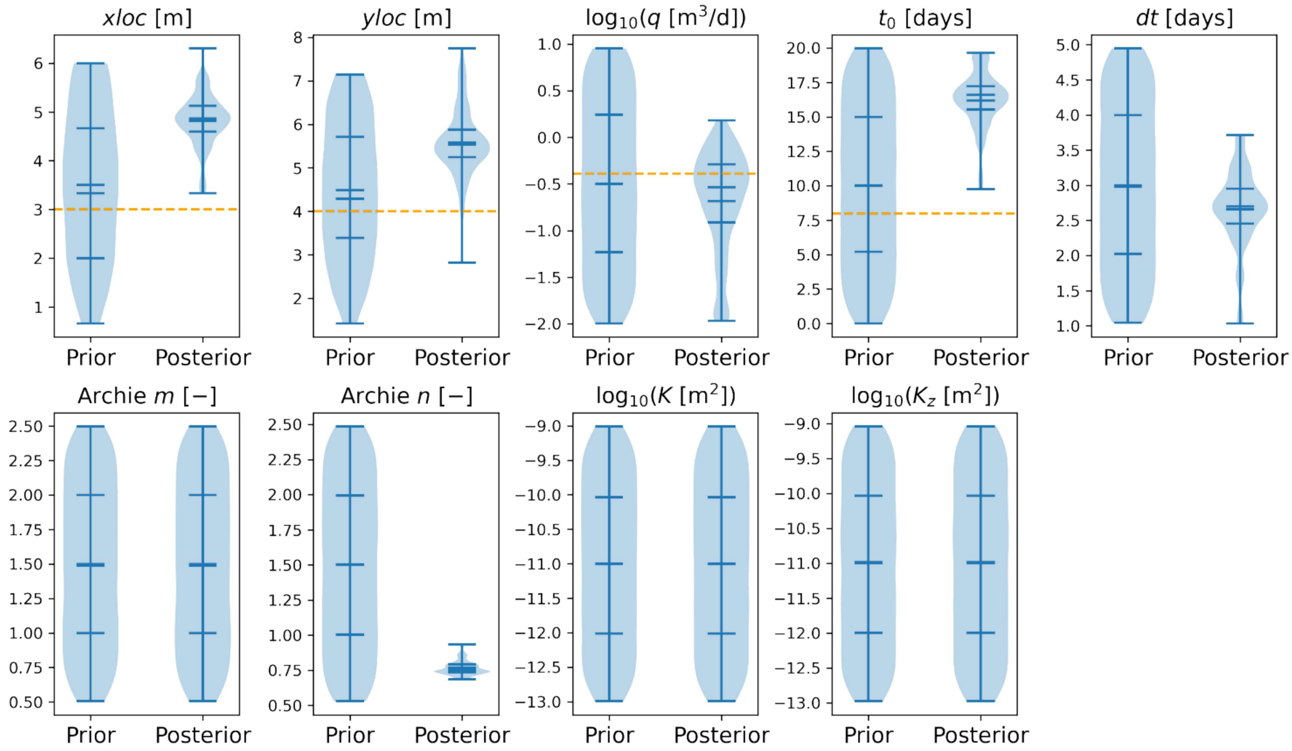

Figure 10 Violin plots showing the prior and posterior parameter values for the Hatfield example estimating leak and Archie parameters and hydraulic conductivities. The parameter symbols and units are defined in Table 3. The true leak parameters used in the field injection experiment is indicated by orange lines.

4.3. Global sensitivity analysis using the Morris method

To better understand the sensitivity of ERT data to various parameters in the coupled hydrogeophysical problem used to analyse the Hatfield dataset, we performed a global sensitivity analysis using the Morris method (Morris, 1991; Tran et al., 2016; Wainwright et al., 2014) that is implemented in the R package *sensitivity* (Iooss, 2019). The Morris method returns the elementary effect (EE) of the parameters, which can be considered as an extension of the local sensitivity method. Since the mean EE represents the average effect of each parameter over the parameter space, the mean EE can be regarded as a global sensitivity measure. To ignore the effects of the sign, the mean of absolute EE is usually reported (mean |EE|). In general, for the parameter ranges considered, parameters with high mean |EE| have a large impact on the data. Unconditional realizations are generated using the Morris algorithm based on the parameter ranges specified in Table 5 and the parameter space is sampled uniformly. We used 25 chains, so for a 13 parameter problem $25 \times (13 + 1) = 350$ realizations are generated. We run the forward models using PFLOTRAN-E4D to obtain simulated ERT response (the settings are the same as those in

Table 4, unless otherwise stated). We set the objective function for calculating the mean |EE| to be the weighted misfit between the simulated and observed ERT data at Hatfield. The same dataset as in the previous section is used.

Results from the global sensitivity analysis of the Hatfield experiment shows that some parameters, especially water table depths and two of the van Genuchten parameters have the largest effects on the data misfit (Table 5), followed by uniform permeability, porosity and Archie parameter values. Leak parameters has low mean |EE|, indicating the difficulty for ERT data to inform their estimation if the others are not known with confidence. Among them, $xloc$ and $yloc$ have the highest and the lowest mean|EE|, respectively. Recharge has virtually no effect on the data misfit. The results show that using ERT data and coupled hydrogeophysical modelling is a challenging problem. Future work can benefit from better constraining the problem incorporating additional data sources (e.g. pressure head, concentration, temperature, saturated and unsaturated hydraulic parameters). Our results agree with that of Tran et al. (2016), who showed Archie parameters have a higher mean |EE| than van Genuchten α. However, they found the mean |EE| of van Genuchten m is negligible, while the largest mean |EE| for ERT data they found is around 8.0. This highlights the Morris sensitivity analysis is best considered on a case-by-case basis, as it is affected by the observed data and the selected parameter ranges. We also report a list of realizations with low data misfit in Table 5. We observe that none of the realizations have an RMSE lower than 7.4 and their parameter values vary greatly. It is noteworthy that a "true" deterministic run (using parameters in Table 3) would give an RMSE of 4.82 (Figure 11). The above shows that some solutions to the ERT leak detection problem can be considered equifinal.

Table 5 Global sensitivity analysis results using the Morris (1991) method on selected parameters on the Hatfield coupled hydrogeophysical model. The parameter ranges considered and the mean absolute elementary effect (|EE|) are reported. Parameter value combinations from ten realizations with the lowest RMSE are also reported.

Parameters [units]	Range	Mean|EE|	#24	#59	#61	#62	#63	#133	#150	#152	#153	#154
xloc [m]	0.0 – 8.0	7.65	0.0	8.0	2.0	2.0	2.0	6.0	2.0	2.0	2.0	2.0
yloc [m]	0.0 – 10.0	0.18	0.0	10.0	2.5	2.5	2.5	10.0	7.5	7.5	7.5	7.5
q [log10 (m^3/d)]	-2.0 – 1.0	1.82	-2.00	-1.25	-1.25	-1.25	-1.25	1.00	-1.25	-1.25	-1.25	-1.25
t0 [d]	0.0 – 20.0	1.53	15.00	5.00	5.00	5.00	5.00	15.00	20.00	20.00	20.00	20.00
Archie m [-]	1.0 – 1.5	26.52	1.38	1.00	1.00	1.00	1.00	1.50	1.50	1.50	1.50	1.50
Archie n [-]	0.5 – 2.0	11.68	1.63	0.88	0.88	0.88	0.88	2.00	1.63	1.63	1.63	1.63
water table [m]	-14.0 – -9.0	49.39	-14.00	-14.00	-14.00	-14.00	-14.00	-14.00	-12.75	-12.75	-12.75	-12.75
permeability [log10 (m^2)]	-15.0 – -12.0	6.85	-15.00	-12.00	-12.00	-14.25	-14.25	-12.00	-12.00	-12.00	-12.00	-12.00
porosity [-]	0.25 – 0.35	12.34	0.25	0.35	0.35	0.35	0.35	0.28	0.35	0.35	0.28	0.28
VG α [Pa^{-1}]	2e-4 – 2e-3	7.50	2.0e-3	2.0e-4	2.0e-4	2.0e-4	1.55e-3	2.0e-4	6.5e-4	6.5e-4	6.5e-4	6.5e-4
VG m [-]	0.4 – 0.8	115.16	0.7	0.7	0.7	0.7	0.7	0.5	0.4	0.7	0.7	0.7
VG Sr [-]	0.01 – 0.2	69.30	0.2	0.01	0.01	0.01	0.01	0.1525	0.01	0.1525	0.1525	0.1525
recharge [mm/d]	0.0 – 0.001	0.03	0.00	7.5e-4	7.5e-4	7.5e-4	7.5e-4	0.00	1.0e-3	1.0e-3	1.0e-3	2.5e-4
RMSE	--	--	7.54	11.10	11.22	11.15	10.57	9.30	8.25	9.40	7.44	7.42

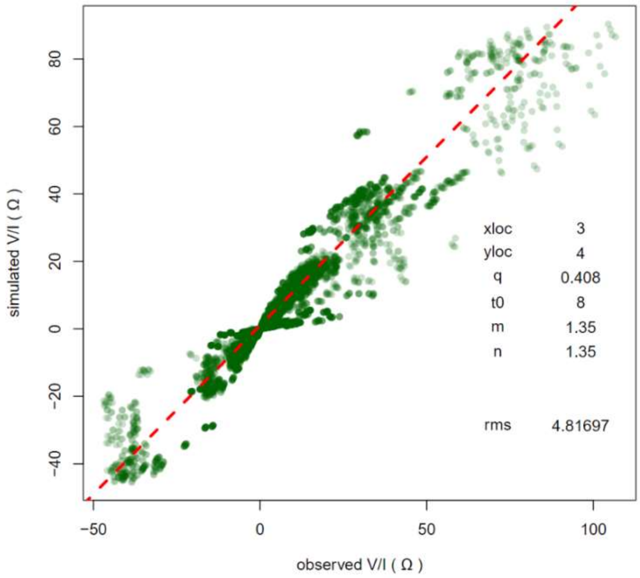

Figure 11 Transfer resistance scatter plot between the observed and simulated data at Hatfield. The simulated data uses parameter values listed in Table 3.

5) Discussion

ERT has been used to detect leaks from nuclear sites for more than two decades. The conventional approach is to use inversion to obtain smoothed images of resistivity at different times and to assess whether there is a leak. This approach does not allow estimation of leak parameters and inversion of large time-lapse ERT datasets can be computationally demanding. We have presented a data assimilation framework to estimate leak parameters from ERT data. It evaluates hydrological model proposals based on the misfits between simulated and observed ERT data and update the model proposals. The estimated leak parameters are presented as a posterior distribution. It also outputs plume mass discharge across a plane, which can be used as a metric to evaluate site-wide uncertainty reduction. These features are not available in existing methods. Since current methods to estimate mass discharge are based on interpolation of point measurements, our coupled modelling approach provides an alternative to quantify mass discharge estimates. Together with point measurements and ERT imaging, the various methods can help establish multiple lines of evidence to better inform decision making in nuclear site characterisation.

Our synthetic results show that the method allows very good estimation of leak parameters (e.g. leak rate, loading size, and location). They also show that this framework can work reasonably well under the influence of uncertain petrophysical parameters and mean K values, as well as under K heterogeneity with small correlation lengths (i.e. with no significant structures). With the rapid growth of autonomous ERT systems to monitor infrastructure, such as British Geological Survey's ALERT and PRIME (Huntley et al., 2019) systems, our approach can provide additional value to ERT data and supplement inverted resistivity images. Our work also has potential to be applied to other non-point source leak detection problems such as seepage through embankments, or using a different geophysical method such as self potential (SP). Likewise, our method could also be applied to induced polarisation (IP) data, which has been shown to be potentially effective for monitoring some reactive plume processes.

We have only examined problems with a few parameters (e.g. leak parameters and homogeneous Archie and permeability values). All hydrological and petrophysical parameters that are not being updated are treated as known constants, which can be strong assumptions on uncertain subsurface properties. Future work should strive to relax such assumption and jointly estimate more parameters. The prior distribution of the uncertain parameters may have an effect on the performance of our data assimilation approach. Nonetheless, we emphasize that they should be chosen based on site-specific prior knowledge. In this work, we have considered a relatively simple problem: a single conservative source with known concentration (thus fluid conductivity) with a single release episode. With the aid of relevant auxiliary information, our framework has the potential to be extended to more complex problems.

The challenges we have encountered when dealing with field data highlights the need of unbiased and reliable prior information for the proposed method to work in practice. Equifinality (Beven, 2006; Binley and Beven, 2003) obviously exist in the leak detection problem since multiple combinations of leak, petrophysical, and hydraulic parameters can give similar data misfits. Different parameterization, scaling of parameters, and additional data sources may alleviate the problem. But ultimately, methods that allow rejection of model proposals may be desirable. Nevertheless, our method can be considered both a quick and approximate method for quantifying posterior uncertainty of parameters of interest, as well as a flexible method to perform regularized inversion without forming the Jacobian (Iglesias, 2016), which can be advantageous for coupled problems. Our proposed method is best used in well characterized sites where an abundance of historical data can be used to build prior models. Alternatively, our method can also be used in controlled tracer injection experiments to estimate hydraulic, petrophysical and transport parameters.

There exists unique challenges for using raw ERT data in data assimilation. ERT datasets are usually quite large, with each timeframe containing hundreds to tens of thousands of data points. The fast collection of ERT data mean that multiple datasets can be collected daily. However, due to computation constraints, we have only used data from a few selected days. Also, each ERT quadrupole measurement neither represent the state response at a point (as in head or concentration data) or the overall system response (as in hydrocarbon production rates). These challenges do not appear to impact leak estimation from synthetic results. But their implications warrant further investigation—for example, can we compress raw ERT data for data assimilation since they may contain significant redundant information?

Frameworks for efficient high-dimensional data assimilation (Ghorbanidehno et al., 2015; Li et al., 2015, 2016) can be used to jointly estimate a heterogeneous permeability field. Methods such as level set methods, discrete cosine transform (DCT) and principal component analysis (PCA) can reduce the number of parameters to describe a highly heterogeneous field. A recent study has applied ES-MDA in combination with level set methods (Iglesias and McLaughlin, 2011; Tai and Chan, 2004) to estimate the three-facies heterogeneous permeability field from conservative tracer test data at the Hanford IFRC site (Song et al., 2019). Future work should explore their utility in hydrogeophysical data assimilation. Likewise, we have assumed relatively simple petrophysical relationships in our coupled hydrogeophysical models. Whether more complex petrophysical models will improve data assimilation results remains an open question. We also have not examined joint assimilation of ERT data with head or concentration data, which can be promising for further constraining our results. In this paper, we have used a relatively small ensemble of highly detailed, fully coupled hydrogeophysical simulations as the forward model. Our work can benefit from a recently developed, adaptive multi-fidelity version of ES-MDA (Zheng et al., 2018), which leverages both the accuracy of highly detailed models and the efficiency of simplified models within the ES-MDA framework.

6) Conclusions

We propose a data assimilation framework that allows the use of time-lapse ERT data for solving hydrological parameters in a leak detection problem. It does not produce any ERT images during inversion; rather, it updates parameters in the hydrological model to minimize ERT data misfit. The use of an ensemble-based framework allows straightforward computation of uncertainty estimates. Site-wide uncertainty reduction can be visualized by comparison of prior and posterior mass discharge curves. Synthetic and field results demonstrate its utility under a variety of settings, e.g. when uniform hydrological and Archie parameters are estimated jointly. This new framework is particularly attractive to sites that have previously undergone extensive geological investigation (e.g., nuclear sites). It can be readily extended to solving other complex problems (e.g. multiple modalities) of interest that is monitored by geophysical data. We have only used ERT data in our analysis but the framework is highly flexible that it is straightforward to incorporate multiple data types. Our method complements electrical resistivity imaging and is particularly applicable to sites where some prior characterization is performed and uncertainty estimates for the parameters that drive the underlying processes observed are desired.

7) Acknowledgement

This paper is published with the permission of the Executive Director of the British Geological Survey (NERC) and Sellafield Ltd. (on behalf of the Nuclear Decommissioning Authority). James Graham and Nick Atherton provided comments that helped improve an earlier version of the manuscript. This work is supported by a Lancaster Environment Centre PhD studentship and a NDA PhD Bursary; the latter enabled the first author’s visits to the PNNL to conduct this work. We thank the PNNL Institutional Computing (PIC) for computing resources. Additional computing resources was provided by the National Energy Research Scientific Computing Center (NERSC), a DOE Office of Science User Facility supported by the Office of Science of the U.S. Department of Energy under Contract No. DE-AC02-05CH11231.

8) References

Aalstad, K., Westermann, S., Schuler, T.V., Boike, J., Bertino, L., 2018. Ensemble-based assimilation of fractional snow-covered area satellite retrievals to estimate the snow distribution at Arctic sites. Cryosphere 12, 247–270. https://doi.org/10.5194/tc-12-247-2018

Abdulsamad, F., Revil, A., Soueid Ahmed, A., Coperey, A., Karaoulis, M., Nicaise, S., Peyras, L., 2019. Induced polarization tomography applied to the detection and the monitoring of leaks in embankments. Eng. Geol. 254, 89–101. https://doi.org/10.1016/J.ENGGEO.2019.04.001

Aghasi, A., Mendoza-Sanchez, I., Miller, E.L., Ramsburg, C.A., Abriola, L.M., 2013. A geometric approach to joint inversion with applications to contaminant source zone characterization. Inverse Probl. 29, 115014. https://doi.org/10.1088/0266-5611/29/11/115014

Audebert, M., Clément, R., Touze-Foltz, N., Günther, T., Moreau, S., Duquennoi, C., 2014. Time-lapse ERT interpretation methodology for leachate injection monitoring based on multiple inversions and a clustering strategy (MICS). J. Appl. Geophys. 111, 320–333. https://doi.org/10.1016/j.jappgeo.2014.09.024

Balbarini, N., Rønde, V., Maurya, P., Fiandaca, G., Møller, I., Erik Klint, K., Christiansen, A. V., Binning, P.J., Bjerg, P.L., 2018. Geophysics Based Contaminant Mass Discharge Quantification Downgradient of a Landfill and a Former Pharmaceutical Factory. Water Resour. Res. https://doi.org/10.1029/2017WR021855

Barnett, D.B., Gee, G.W., Sweeney, M.D., Johnson, M.D., Medina, V.F., Khan, F., 2003. Results of Performance Evaluation Testing of Electrical Leak-Detection Methods at the Hanford Site Mock Tank – FY 2002-2003. Richland, Washington.

Beven, K., 2006. A manifesto for the equifinality thesis. J. Hydrol. 320, 18–36. https://doi.org/10.1016/j.jhydrol.2005.07.007

Binley, A., Beven, K., 2003. Vadose zone flow model uncertianty as conditioned on geophysical data. Groundwater 41, 119–127.

Binley, A., Cassiani, G., Middleton, R., Winship, P., 2002. Vadose zone flow model parameterisation using cross-borehole radar and resistivity imaging. J. Hydrol. 267, 147–159. https://doi.org/10.1016/S0022-1694(02)00146-4

Binley, A., Hubbard, S.S., Huisman, J.A., Revil, A., Robinson, D.A., Singha, K., Slater, L.D., 2015. The emergence of hydrogeophsyics for improved understanding of subsurface processes over multiple scales. Water Resour. Res. 51, 3837–3866. https://doi.org/10.1002/2015WR017016

Binley, A., Winship, P., Middleton, R., Pokar, M., West, J., 2001. High-resolution characterization of vadose zone dynamics using cross-borehole radar. Water Resour. Res. 37, 2639–2652. https://doi.org/10.1029/2000WR000089

Brusseau, M.L., Guo, Z., 2014. Assessing contaminant-removal conditions and plume persistence through analysis of data from long-term pump-and-treat operations. J. Contam. Hydrol. 164, 16–24. https://doi.org/10.1016/j.jconhyd.2014.05.004

Cai, Z., Wilson, R.D., Cardiff, M.A., Kitanidis, P.K., 2011. Increasing Confidence in Mass Discharge Estimates Using Geostatistical Methods. Ground Water 49, 197–208. https://doi.org/10.1111/j.1745-6584.2010.00709.x

Camporese, M., Cassiani, G., Deiana, R., Salandin, P., 2011. Assessment of local hydraulic properties from electrical resistivity tomography monitoring of a three-dimensional synthetic tracer test experiment. Water Resour. Res. 47, 1–15. https://doi.org/10.1029/2011WR010528

Camporese, M., Cassiani, G., Deiana, R., Salandin, P., Binley, A., 2015. Coupled and uncoupled hydrogeophysical inversions using ensemble Kalman filter assimilation of ERT-monitored tracer test data. Water Resour. Res. 51, 3277–3291. https://doi.org/10.1002/2014WR016017

Chambers, J.E., Kuras, O., Meldrum, P.I., Ogilvy, R.D., Hollands, J., 2006. Electrical resistivity tomography applied to geologic, hydrogeologic, and engineering investigations at a former waste-disposal site. Geophysics 71, B231–B239. https://doi.org/10.1190/1.2360184

Chen, X., Hammond, G.E., Murray, C.J., Rockhold, M.L., Vermeul, V.R., Zachara, J.M., 2013. Application of ensemble-based data assimilation techniques for aquifer characterization using tracer data at Hanford 300 area. Water Resour. Res. 49, 7064–7076. https://doi.org/10.1002/2012WR013285

Chen, Z., Gómez-Hernández, J.J., Xu, T., Zanini, A., 2018. Joint identification of contaminant source and aquifer geometry in a sandbox experiment with the restart ensemble Kalman filter. J. Hydrol. 564, 1074–1084. https://doi.org/10.1016/J.JHYDROL.2018.07.073

Christ, J.A., Ramsburg, C.A., Pennell, K.D., Abriola, L.M., 2010. Predicting DNAPL mass discharge from pool-dominated source zones. J. Contam. Hydrol. https://doi.org/10.1016/j.jconhyd.2010.02.005

Christ, J.A., Ramsburg, C.A., Pennell, K.D., Abriola, L.M., 2006. Estimating mass discharge from dense nonaqueous phase liquid source zones using upscaled mass transfer coefficients: An evaluation using multiphase numerical simulations. Water Resour. Res. 42, 1–13. https://doi.org/10.1029/2006WR004886

Crestani, E., Camporese, M., Salandin, P., 2015. Assessment of hydraulic conductivity distributions through assimilation of travel time data from ERT-monitored tracer tests. Adv. Water Resour. 84, 23–36. https://doi.org/10.1016/j.advwatres.2015.07.022

Daily, W., Ramirez, A., Binley, A., 2004. Remote monitoring of leaks in storage tanks using electrical resistance tomography: Application at the Hanford Site. J. Environ. Eng. Geophys. 9, 11–24. https://doi.org/10.4133/jeeg9.1.11

Datta, B., Chakrabarty, D., Dhar, A., 2009. Simultaneous identification of unknown groundwater pollution sources and estimation of aquifer parameters. J. Hydrol. 376, 48–57. https://doi.org/10.1016/J.JHYDROL.2009.07.014

Emerick, A.A., Reynolds, A.C., 2013. Ensemble smoother with multiple data assimilation. Comput. Geosci. 55, 3–15. https://doi.org/10.1016/j.cageo.2012.03.011

Ghorbanidehno, H., Kokkinaki, A., Li, J.Y., Darve, E., Kitanidis, P.K., 2015. Real-time data assimilation for large-scale systems: The spectral Kalman filter. Adv. Water Resour. 86, 260–272. https://doi.org/10.1016/j.advwatres.2015.07.017

Hadley, P.W., Newell, C.J., 2012. Groundwater Remediation: The Next 30 Years. Ground Water 50, 669–678. https://doi.org/10.1111/j.1745-6584.2012.00942.x

Hammond, G.E., Lichtner, P.C., 2010. Field-scale model for the natural attenuation of uranium at the Hanford 300 Area using high-performance computing. Water Resour. Res. 46, 1–31. https://doi.org/10.1029/2009WR008819

Hermans, T., Nguyen, F., Caers, J., 2015. Uncertainty in training image-based inversion of hydraulic head data constrained to ERT data:Workflow and case study. Water Resour. Res. 51, 5332–5352. https://doi.org/10.1002/2014WR016259

Hermans, T., Oware, E., Caers, J., 2016. Direct prediction of spatially and temporally varying physical properties from time-lapse electrical resistance data. Water Resour. Res. 52, 7262–7283. https://doi.org/10.1002/2016WR019126

Hinnell, A.C., Ferr, T.P.A., Vrugt, J.A., Huisman, J.A., Moysey, S., Rings, J., Kowalsky, M.B., 2010. Improved extraction of hydrologic information from geophysical data through coupled hydrogeophysical inversion. Water Resour. Res. 46, 1–14. https://doi.org/10.1029/2008WR007060

Huntley, D., Bobrowsky, P., Hendry, M., Macciotta, R., Elwood, D., Sattler, K., Best, M., Chambers, J., Meldrum, P., 2019. Application of multi-dimensional electrical resistivity tomography datasets to investigate a very slow-moving landslide near Ashcroft, British Columbia, Canada. Landslides 16, 1033–1042. https://doi.org/10.1007/s10346-019-01147-1

Iglesias, M.A., 2016. A regularizing iterative ensemble Kalman method for PDE-constrained inverse problems. Inverse Probl. 32, 025002. https://doi.org/10.1088/0266-5611/32/2/025002

Iglesias, M.A., McLaughlin, D., 2011. Level-set techniques for facies identification in reservoir modeling. Inverse Probl. 27, 36. https://doi.org/10.1088/0266-5611/27/3/035008

Iooss, B., 2019. Package ‘sensitivity.’

Irving, J., Singha, K., 2010. Stochastic inversion of tracer test and electrical geophysical data to estimate hydraulic conductivities. Water Resour. Res. 46, W11514. https://doi.org/10.1029/2009WR008340

ITRC, 2010. Use and Measurement of Mass Flux and Mass Discharge, Use and Measurement of Mass Flux and Mass Discharge. Washington DC.

Johnson, T.C., Hammond, G.E., Chen, X., 2017. PFLOTRAN-E4D: A parallel open source PFLOTRAN module for simulating time-lapse electrical resistivity data. Comput. Geosci. 99, 72–80. https://doi.org/10.1016/j.cageo.2016.09.006

Johnson, T.C., Rucker, D.F., Glaser, D.R., 2015a. Near-Surface Geophysics at the Hanford Nuclear Site, the United States, in: Treatise on Geophysics. Elsevier, pp. 571–595. https://doi.org/10.1016/B978-0-444-53802-4.00205-0

Johnson, T.C., Slater, L.D., Ntarlagiannis, D., Day-Lewis, F.D., Elwaseif, M., 2012. Monitoring groundwater-surface water interaction using time-series and time-frequency analysis of transient three-dimensional electrical resistivity changes. Water Resour. Res. 48, 1–13. https://doi.org/10.1029/2012WR011893

Johnson, T.C., Versteeg, R., Thomle, J., Hammond, G., Chen, X., Zachara, J., 2015b. Four-dimensional electrical conductivity monitoring of stage-driven river water intrusion: Accounting for water table effects using a transient mesh boundary and conditional inversion constraints. Water Resour. Res. 51, 6177–6196. https://doi.org/10.1002/2014WR016129

Johnson, T.C., Versteeg, R.J., Day-Lewis, F.D., Major, W., Lane, J.W., 2015c. Time-Lapse Electrical Geophysical Monitoring of Amendment-Based Biostimulation. Groundwater 53, 920–932. https://doi.org/10.1111/gwat.12291

Johnson, T.C., Versteeg, R.J., Huang, H., Routh, P.S., 2009. Data-domain correlation approach for joint hydrogeologic inversion of time-lapse hydrogeologic and geophysical data. Geophysics 74, F127. https://doi.org/10.1190/1.3237087

Johnson, T.C., Versteeg, R.J., Ward, A., Day-Lewis, F.D., Revil, A., 2010. Improved hydrogeophysical characterization and monitoring through parallel modeling and inversion of time-domain resistivity and induced-polarization data. Geophysics 75, WA27. https://doi.org/10.1190/1.3475513

Johnson, T.C., Wellman, D., 2015. Accurate modelling and inversion of electrical resistivity data in the presence of metallic infrastructure with known location and dimension. Geophys. J. Int. 202, 1096–1108. https://doi.org/10.1093/gji/ggv206

Ju, L., Zhang, J., Meng, L., Wu, L., Zeng, L., 2018. An adaptive Gaussian process-based iterative ensemble smoother for data assimilation. Adv. Water Resour. https://doi.org/10.1016/j.advwatres.2018.03.010

Kang, X., Shi, X., Deng, Y., Revil, A., Xu, H., Wu, J., 2018. Coupled hydrogeophysical inversion of DNAPL source zone architecture and permeability field in a 3D heterogeneous sandbox by assimilation time-lapse cross-borehole electrical resistivity data via ensemble Kalman filtering. J. Hydrol. 567, 149–164. https://doi.org/10.1016/j.jhydrol.2018.10.019

Kang, X., Shi, X., Revil, A., Cao, Z., Li, L., Lan, T., Wu, J., 2019. Coupled hydrogeophysical inversion to identify non-Gaussian hydraulic conductivity field by jointly assimilating geochemical and time-lapse geophysical data. J. Hydrol. https://doi.org/10.1016/j.jhydrol.2019.124092

Koch, J., Nowak, W., 2016. Identification of contaminant source architectures—A statistical inversion that emulates multiphase physics in a computationally practicable manner. Water Resour. Res. 52. https://doi.org/10.1002/2014WR015716

Köpke, C., Elsheikh, A.H., Irving, J., 2019. Hydrogeophysical Parameter Estimation Using Iterative Ensemble Smoothing and Approximate Forward Solvers. Front. Environ. Sci. 7, 34. https://doi.org/10.3389/fenvs.2019.00034

Kowalsky, M.B., Finsterle, S., Peterson, J., Hubbard, S., Rubin, Y., Majer, E., Ward, A., Gee, G., 2005. Estimation of field-scale soil hydraulic and dielectric parameters through joint inversion of GPR and hydrological data. Water Resour. Res. 41, n/a-n/a. https://doi.org/10.1029/2005WR004237

Kuras, O., Pritchard, J.D., Meldrum, P.I., Chambers, J.E., Wilkinson, P.B., Ogilvy, R.D., 2009. Monitoring hydraulic processes with Automated time-Lapse Electrical Resistivity Tomography (ALERT). Comptes Rendus Geosci. 351, 868–885.

Kuras, O., Wilkinson, P.B., Meldrum, P.I., Oxby, L.S., Uhlemann, S., Chambers, J.E., Binley, A., Graham, J., Smith, N.T., Atherton, N., 2016. Geoelectrical monitoring of simulated subsurface leakage to support high-hazard nuclear decommissioning at the Sellafield Site, UK. Sci. Total Environ. 566–567, 350–359. https://doi.org/10.1016/j.scitotenv.2016.04.212

Kwong, S., Fowler, L., 2014. Technical Memorandum: MSSS Electrical Resistivity Tomography (ERT): TRAFFIC modelling of the ERT trial.

LaBrecque, D.J., Ramirez, A.L., Daily, W.D., Binley, A.M., Schima, S.A., 1996. ERT monitoring on environmental remediation processes. Meas. Sci. Technol. 7, 375–383. https://doi.org/10.1088/0957-0233/7/3/019

Lan, T., Shi, X., Jiang, B., Sun, Y., Wu, J., 2018. Joint inversion of physical and geochemical parameters in groundwater models by sequential ensemble-based optimal design. Stoch. Environ. Res. Risk Assess. 5. https://doi.org/10.1007/s00477-018-1521-5

Le, D.H., Emerick, A.A., Reynolds, A.C., 2016. An Adaptive Ensemble Smoother With Multiple Data Assimilation for Assisted History Matching. SPE J. 21, 2195–2207. https://doi.org/10.2118/173214-PA

Li, J.Y., Kokkinaki, A., Ghorbanidehno, H., Darve, E.F., Kitanidis, P.K., 2015. The compressed state Kalman filter for nonlinear state estimation: Application to large-scale reservoir monitoring. Water Resour. Res. 51, 9942–9963. https://doi.org/10.1002/2015WR017203

Li, L., Puzel, R., Davis, A., 2018. Data assimilation in groundwater modelling: ensemble Kalman filter versus ensemble smoothers. Hydrol. Process. 32, 2020–2029. https://doi.org/10.1002/hyp.13127

Li, Y.J., Kokkinaki, A., Darve, E.F., 2016. Smoothing-based compressed state Kalman filter for joint state-parameter estimation : applications in reservoir characterization and CO 2 storage monitoring. Water Resour. Res. 53, 7190–7207. https://doi.org/10.1002/2016WR020168

Manoli, G., Rossi, M., Pasetto, D., Deiana, R., Ferraris, S., Cassiani, G., Putti, M., 2015. An iterative particle filter approach for coupled hydro-geophysical inversion of a controlled infiltration experiment. J. Comput. Phys. 283, 37–51. https://doi.org/10.1016/J.JCP.2014.11.035

Mariethoz, G., Renard, P., Straubhaar, J., 2010. The direct sampling method to perform multiple-point geostatistical simulations. Water Resour. Res. 46, 1–14. https://doi.org/10.1029/2008WR007621

Maurya, P.K., Rønde, V.K., Fiandaca, G., Balbarini, N., Auken, E., Bjerg, P.L., Christiansen, A.V., 2017. Detailed landfill leachate plume mapping using 2D and 3D electrical resistivity tomography - with correlation to ionic strength measured in screens. J. Appl. Geophys. 138, 1–8. https://doi.org/10.1016/j.jappgeo.2017.01.019

Michalak, A.M., Shlomi, S., 2007. A geostatistical data assimilation approach for estimating groundwater plume distributions from multiple monitoring events. pp. 73–88. https://doi.org/10.1029/171GM08

Millard, S.P., 2013. Designing a Sampling Program. EnvStats An R Packag. Environ. Stat. 25–61. https://doi.org/10.1007/978-1-4614-8456-1

Morris, M.D., 1991. Factorial Sampling Plans for Preliminary Computational Experiments, Technometrics.

Nowak, W., 2009. Best unbiased ensemble linearization and the quasi-linear Kalman ensemble generator. Water Resour. Res. 45. https://doi.org/10.1029/2008WR007328

Oware, E.K., Moysey, S.M.J., Khan, T., 2013. Physically based regularization of hydrogeophysical inverse problems for improved imaging of process-driven systems. Water Resour. Res. 49, 6238–6247. https://doi.org/10.1002/wrcr.20462

Pidlisecky, A., Singha, K., Day-Lewis, F.D., 2011. A distribution-based parametrization for improved tomographic imaging of solute plumes. Geophys. J. Int. 187, 214–224. https://doi.org/10.1111/j.1365-246X.2011.05131.x

Power, C., Gerhard, J.I., Karaoulis, M., Tsourlos, P., Giannopoulos, A., 2014. Evaluating four-dimensional time-lapse electrical resistivity tomography for monitoring DNAPL source zone remediation. J. Contam. Hydrol. 162–163, 27–46. https://doi.org/10.1016/j.jconhyd.2014.04.004

Ramirez, A., Daily, W., Binley, A., Labrecque, D., Roelant, D., 1996. Detection of leaks in underground storage tanks using electrical resistance methods. J. Environ. Eng. Geophys. 1, 189–203. https://doi.org/10.4133/JEEG1.3.189

Ramirez, A.L., Nitao, J.J., Hanley, W.G., Aines, R., Glaser, R.E., Sengupta, S.K., Dyer, K.M., Hickling, T.L., Daily, W.D., 2005. Stochastic inversion of electrical resistivity changes using a Markov Chain Monte Carlo approach. J. Geophys. Res. Solid Earth 110, B02101. https://doi.org/10.1029/2004JB003449

Reynolds, A.C., Zafari, M., Li, G., 2006. Iterative forms of the ensemble Kalman filter, in: Proceedings of 10th European Conference on the Mathematics of Oil Recovery. Amsterdam, The Netherlands.

Rossi, M., Manoli, G., Pasetto, D., Deiana, R., Ferraris, S., Strobbia, C., Putti, M., Cassiani, G., 2015. Coupled inverse modeling of a controlled irrigation experiment using multiple hydro-geophysical data. Adv. Water Resour. 82, 150–165. https://doi.org/10.1016/J.ADVWATRES.2015.03.008

Scholer, M., Irving, J., Looms, M.C., Nielsen, L., Holliger, K., 2012. Bayesian Markov-chain-Monte-Carlo inversion of time-lapse crosshole GPR data to characterize the vadose zone at the Arrenaes site, Denmark. (Special Section: Model-data fusion in the vadose zone.). Vadose Zo. J. 11, 153. https://doi.org/10.2136/vzj2011.0153

Schöniger, A., Nowak, W., Hendricks Franssen, H.-J., 2012. Parameter estimation by ensemble Kalman filters with transformed data: Approach and application to hydraulic tomography. Water Resour. Res. 48, W04502. https://doi.org/10.1029/2011WR010462

Shlomi, S., Michalak, A.M., 2007. A geostatistical framework for incorporating transport information in estimating the distribution of a groundwater contaminant plume. Water Resour. Res. 43. https://doi.org/10.1029/2006WR005121

Singha, K., Gorelick, S.M., 2006. Effects of spatially variable resolution on field-scale estimates of tracer concentration from electrical inversions using Archie's law. Geophysics 71, G83. https://doi.org/10.1190/1.2194900

Slater, L., Binley, A., 2006. Synthetic and field-based electrical imaging of a zerovalent iron barrier: Implications for monitoring long-term barrier performance. Geophysics 71, B129–B137. https://doi.org/10.1190/1.2235931

Slater, L., Binley, A., 2003. Evaluation of permeable reactive barrier (PRB) integrity using electrical imaging methods. Geophysics 68, 911–921. https://doi.org/10.1190/1.1581043

Slater, L.D., Ntarlagiannis, D., Day-Lewis, F.D., Mwakanyamale, K., Versteeg, R.J., Ward, A., Strickland, C., Johnson, C.D., Lane, J.W., 2010. Use of electrical imaging and distributed temperature sensing methods to characterize surface water-groundwater exchange regulating uranium transport at the Hanford 300 Area, Washington. Water Resour. Res. 46, 1–13. https://doi.org/10.1029/2010WR009110

Song, X., Chen, X., Ye, M., Dai, Z., Hammond, G., Zachara, J.M., 2019. Delineating Facies Spatial Distribution by Integrating Ensemble Data Assimilationand Indicator Geostatistics With Level-Set Transformation. Water Resour. Res. 2018WR023262. https://doi.org/10.1029/2018WR023262

Sun, A.Y., 2007. A robust geostatistical approach to contaminant source identification. Water Resour. Res. https://doi.org/10.1029/2006WR005106

Sun, A.Y., Painter, S.L., Wittmeyer, G.W., 2006. A constrained robust least squares approach for contaminant release history identification. Water Resour.

Res. 42. https://doi.org/10.1029/2005WR004312

Sun, N.-Z., Sun, A., 2015. Model Calibration and Parameter Estimation. Springer New York, New York, NY. https://doi.org/10.1007/978-1-4939-2323-6

Tai, X., Chan, T.F., 2004. A survey on multiple level set methods with applications for identifying piecewise constant functions. Int. J. Numer. Anal. Model 1, 25–48.

Tran, A.P., Dafflon, B., Hubbard, S.S., Kowalsky, M.B., Long, P., Tokunaga, T.K., Williams, K.H., 2016. Quantifying shallow subsurface water and heat dynamics using coupled hydrological-thermal-geophysical inversion. Hydrol. Earth Syst. Sci. 20, 3477–3491. https://doi.org/10.5194/hess-20-3477-2016

Troldborg, M., Nowak, W., Lange, I. V., Santos, M.C., Binning, P.J., Bjerg, P.L., 2012. Application of Bayesian geostatistics for evaluation of mass discharge uncertainty at contaminated sites. Water Resour. Res. 48, 1–19. https://doi.org/10.1029/2011WR011785

Troldborg, M., Nowak, W., Tuxen, N., Bjerg, P.L., Helmig, R., Binning, P.J., 2010. Uncertainty evaluation of mass discharge estimates from a contaminated site using a fully Bayesian framework. Water Resour. Res. 46, 1–19. https://doi.org/10.1029/2010WR009227

Truex, M.J., Johnson, T.C., Strickland, C.E., Peterson, J.E., Hubbard, S.S., 2013. Monitoring Vadose Zone Desiccation with Geophysical Methods. Vadose Zo. J. 12. https://doi.org/10.2136/vzj2012.0147

Truex, M.J., Oostrom, M., Strickland, C.E., Chronister, G.B., Benecke, M.W., Johnson, C.D., 2012. Field-Scale Assessment of Desiccation Implementation for Deep Vadose Zone Contaminants. Vadose Zo. J. 11, 0. https://doi.org/10.2136/vzj2011.0144

Tso, C.-H.M., Kuras, O., Wilkinson, P.B., Uhlemann, S., Chambers, J.E., Meldrum, P.I., Graham, J., Sherlock, E.F., Binley, A., 2017. Improved characterisation and modelling of measurement errors in electrical resistivity tomography (ERT) surveys. J. Appl. Geophys. 146, 103–119. https://doi.org/10.1016/J.JAPPGEO.2017.09.009

Wagner, B.J., 1992. Simultaneous parameter estimation and contaminant source characterization for coupled groundwater flow and contaminant transport modelling. J. Hydrol. 135, 275–303. https://doi.org/10.1016/0022-1694(92)90092-A

Wainwright, H.M., Finsterle, S., Jung, Y., Zhou, Q., Birkholzer, J.T., 2014. Making sense of global sensitivity analyses. Comput. Geosci. 65, 84–94. https://doi.org/10.1016/j.cageo.2013.06.006

Wallin, E.L., Johnson, T.C., Greenwood, W.J., Zachara, J.M., 2013. Imaging high stage river-water intrusion into a contaminated aquifer along a major river corridor using 2-D time-lapse surface electrical resistivity tomography. Water Resour. Res. 49, 1693–1708. https://doi.org/10.1002/wrcr.20119

Ward, W.O.C., Wilkinson, P.B., Chambers, J.E., Nilsson, H., Kuras, O., Bai, L., 2016. Tracking tracer motion in a 4-D electrical resistivity tomography experiment. Water Resour. Res. 52, 4078–4094. https://doi.org/10.1002/2015WR017958

Winship, P., Binley, A., Gomez, D., 2006. Flow and transport in the unsaturated Sherwood Sandstone: characterization using cross-borehole geophysical methods. Geol. Soc. London, Spec. Publ. 263, 219–231. https://doi.org/10.1144/GSL.SP.2006.263.01.12

Xu, T., Gómez-Hernández, J.J., 2018. Simultaneous identification of a contaminant source and hydraulic conductivity via the restart normal-score ensemble Kalman filter. Adv. Water Resour. 112, 106–123. https://doi.org/10.1016/j.advwatres.2017.12.011

Xu, T., Gómez-Hernández, J.J., 2016. Joint identification of contaminant source location, initial release time, and initial solute concentration in an aquifer via ensemble Kalman filtering. Water Resour. Res. 52, 6587–6595. https://doi.org/10.1002/2016WR019111

Zeng, L., Shi, L., Zhang, D., Wu, L., 2012. A sparse grid based Bayesian method for contaminant source identification. Adv. Water Resour. 37, 1–9. https://doi.org/10.1016/J.ADVWATRES.2011.09.011

Zheng, Q., Zhang, J., Xu, W., Wu, L., Zeng, L., 2018. Adaptive Multi-Fidelity Data Assimilation for Nonlinear Subsurface Flow Problems. Water Resour. Res. 2018WR023615. https://doi.org/10.1029/2018WR023615

Zhou, H., Gómez-Hernández, J.J., Li, L., 2014. Inverse methods in hydrogeology: Evolution and recent trends. Adv. Water Resour. 63, 22–37. https://doi.org/10.1016/j.advwatres.2013.10.014

Zovi, F., Camporese, M., Hendricks Franssen, H.J., Huisman, J.A., Salandin, P., 2017. Identification of high-permeability subsurface structures with multiple point geostatistics and normal score ensemble Kalman filter. J. Hydrol. 548, 208–224. https://doi.org/10.1016/j.jhydrol.2017.02.056